Atmos. Chem. Phys. Discuss., 7, 8035–8085, 2007
www.atmos-chem-phys-discuss.net/7/8035/2007/

Atmospheric Chemistry and Physics Discussions

Cloud-scale model intercomparison of chemical constituent transport in deep convection

M. C. Barth[1], S.-W. Kim[1,*], C. Wang[2], K. E. Pickering[3,], L. E. Ott[3,**], G. Stenchikov[4], M. Leriche[5,***], S. Cautenet[5], J.-P. Pinty[6], Ch. Barthe[6], C. Mari[6], J. Helsdon[7], R. Farley[7], A. M. Fridlind[8,****], A. S. Ackerman[8,****], V. Spiridonov[9], and B. Telenta[10]**

[1]National Center for Atmospheric Research, Boulder, Colorado, USA
[2]Massachusetts Institute of Technology, Cambridge, Massachusetts, USA
[3]University of Maryland, College Park, Maryland, USA
[4]Rutgers University, New Brunswick, New Jersey, USA
[5]CNRS/University Blaise-Pascal, Clermont-Ferrand, France
[6]CNRS/Paul Sabatier University, Toulouse, France
[7]South Dakota School of Mines and Technology, Rapid City, South Dakota, USA
[8]NASA-Ames Research Center, Moffett Field, California, USA
[9]Hydrometeorological Institute, Skopje, Macedonia
[10]SENES Consultant Ltd., Toronto, Canada
[*]now at: ESRL/CSD and CIRES, University of Colorado, Boulder, Colorado, USA
[**]now at: NASA-Goddard Space Flight Center, Greenbelt, Maryland, USA

*** now at: CNRS/Paul Sabatier University, Toulouse, France
**** now at: NASA-GISS, New York City, New York, USA

Received: 14 May 2007 – Accepted: 27 May 2007 – Published: 8 June 2007

Correspondence to: M. C. Barth (barthm@ucar.edu)

Abstract

Transport and scavenging of chemical constituents in deep convection is important to understanding the composition of the troposphere and therefore chemistry-climate and air quality issues. High resolution cloud chemistry models have been shown to represent convective processing of trace gases quite well. To improve the representation of sub-grid convective transport and wet deposition in large-scale models, general characteristics, such as species mass flux, from the high resolution cloud chemistry models can be used. However, it is important to understand how these models behave when simulating the same storm. The intercomparison described here examines transport of six species. CO and O_3, which are primarily transported, show good agreement among models and compare well with observations. Models that included lightning production of NO_x reasonably predict NO_x mixing ratios in the anvil compared with observations, but the NO_x variability is much larger than that seen for CO and O_3. Predicted anvil mixing ratios of the soluble species, HNO_3, H_2O_2, and CH_2O, exhibit significant differences among models, attributed to different schemes in these models of cloud processing including the role of the ice phase, the impact of cloud-modified photolysis rates on the chemistry, and the representation of the species chemical reactivity. The lack of measurements of these species in the convective outflow region does not allow us to evaluate the model results with observations.

1 Introduction

Convective processing of trace gas species is an important means of moving chemical constituents rapidly between the boundary layer and free troposphere, and is also an effective way of cleansing the atmosphere through wet deposition. Because of these two processes, the effect of convection on chemical species is critical to our understanding of chemistry-climate studies, air quality studies, and the effects of acidic precipitation on the earth's surface.

ACPD

7, 8035–8085, 2007

In large-scale models convective parameterizations have been developed primarily on the basis of mass and heat fluxes. An intercomparison of several convective parameterizations used in both global and regional scale models shows that there is significant variability among the parameterizations (Xie et al., 2002; Tost et al., 2006). Lawrence and Rasch (2005) compared tracer transport in deep convection for plume ensemble and bulk formulations of convective transport parameterizations. Their results showed differences in the upper troposphere of up to 25% between the plume ensemble and bulk formulations of convective transport for the July monthly mean mixing ratios of decaying, insoluble scalars. At shorter averaging times, the differences between the two formulations are even greater. Clearly there is a need to improve the parameterizations of trace gas transport by convection in the global models.

On the other hand, many previous studies using high resolution cloud-resolving models (or convective cloud models) have shown that case-specific simulations are able to represent the storm structure and kinematics, such as radar reflectivity, wind speed and direction, and outflow heights. Convective cloud models coupled with chemistry simulate the redistribution of passive trace gas species well (e.g. Pickering et al., 1996; Stenchikov et al., 1996; Wang and Prinn, 2000; Skamarock et al., 2000; DeCaria et al., 2000). The cloud-resolving models, when incorporated with reasonably comprehensive chemistry, can also provide details of cloud processing of soluble chemical species as well as tropospheric production/destruction of short-lived species including critical hydrogen oxides precursors and aerosols influenced by the existence of convection (e.g., Wang and Chang 1993b, c; Wang and Crutzen, 1995; Wang and Prinn, 2000; Barth et al., 2001, 2007; Ekman et al., 2004, 2006, DeCaria et al., 2005). Adequate representation of cloud processing of reactive and soluble species in the large scale models is still in demand.

Convective transport and wet deposition of chemical species in large-scale models are sub-grid scale processes and thus have to be implicitly represented by various parameterizations using grid resolving variables. To improve these parameterizations, the high resolution and process-oriented convective-scale model can be used to obtain

general characteristics of these sub-grid processes in particular when multiple cloud resolving models are involved. Before gathering convective transport characteristics of tracers from multiple cloud resolving model simulations of different storms, it is important to understand how these models behave when simulating the same storm. Results presented here as part of the 6th International Cloud Modeling Workshop (Grabowski, 2006) Case 5 intercomparison provide a means to make an initial comparison of a variety of cloud resolving models coupled with chemistry.

The Chemistry Transport by Deep Convection Intercomparison case was designed to assess the capability of each model to transport different chemical species from the boundary layer to the upper troposphere including the entrainment of free tropospheric air. Parameterizations of lightning-produced NO_x are part of the intercomparison exercise. Carbon monoxide (CO) and ozone (O_3) are compared as tracers of transport because the lifetime of the storm (hours) is shorter than the chemical lifetime of these species. Nitrogen oxides (NO_x = NO + NO_2) are examined to assess transformation, transport, and NO_x production by lightning. Nitric acid (HNO_3), hydrogen peroxide (H_2O_2), and formaldehyde (CH_2O) are compared to evaluate chemical transformation and transport of soluble and reactive species.

2 Description of the case

The 10 July 1996 STERAO case was observed near the Wyoming-Nebraska-Colorado border. The isolated storm evolved from a multicellular thunderstorm to a quasi-supercell. Observations of the storm were obtained from several platforms including the CSU CHILL radar, the ONERA lightning interferometers, the NOAA WP3D aircraft, and the UND Citation aircraft. These observations are summarized by Dye et al. (2000).

The simulations performed for the intercomparison mimic those described by Skamarock et al. (2000) and Barth et al. (2001, 2007). The environment was assumed to be homogeneous, thus a single profile was used for initialization. The initial profiles

of the meteorological data were obtained from sonde and aircraft data (Skamarock et al., 2000). To start the convection quickly so that the intercomparison could focus on chemical species transport, the convection was initiated with 3 warm bubbles (3°C perturbation) oriented in a NW to SE line. Simulations were integrated for a 3-h period.

The initial profiles (Fig. 1) of the chemical species are primarily from the aircraft observations obtained outside of cloud. CO is a surface tracer with a surface mixing ratio of 135 nmol mol^{-1}. CO mixing ratios in the free troposphere range from 90–110 nmol mol^{-1} in the mid-troposphere and 50–90 nmol mol^{-1} in the upper troposphere. O_3 mixing ratios are fairly constant with height to about 7 km mean sea level (m.s.l.), above which O_3 mixing ratios rapidly increase into the stratosphere. The initial profile of NO_x is based on NO measurements outside of cloud. NO_x mixing ratios are ~500 pmol mol^{-1} near the surface, but quickly decrease to values near 50 pmol mol^{-1} in the mid troposphere. At high altitudes NO_x increases to 200 pmol mol^{-1}. CH_2O and H_2O_2 initial mixing ratios are from the low-flying aircraft that are combined with values obtained from the literature for high altitudes. CH_2O decreases from the surface to <200 pmol mol^{-1} in the mid-troposphere. H_2O_2 mixing ratios peak near the top of the boundary layer then rapidly decrease in the mid to upper troposphere. HNO_3 mixing ratios are based on NO_y measurements from the NASA SUCCESS (Jaeglé et al., 1998) and the NSF ELCHEM (Ridley et al., 1994) field campaigns.

3 Description of the models used in the intercomparison

Eight modeling groups submitted results for comparison. Tables 1 and 2 identify each group and key characteristics of their models. Details of model characteristics are discussed here.

3.1 WRF with aqueous chemistry (WRF-AqChem, Mary Barth and Si-Wan Kim)

A simple gas and aqueous chemistry scheme has been incorporated into the Weather Research and Forecasting (WRF) model (Barth et al., 2007). The WRF model solves the conservative (flux-form), nonhydrostatic compressible equations using a split-explicit time-integration method based on a 3rd order Runge-Kutta scheme (Skamarock et al., 2005; Wicker and Skamarock, 2002). Scalar transport is integrated with the Runge-Kutta scheme using 5th order (horizontal) and 3rd order (vertical) upwind-biased advection operators. Transported scalars include water vapor, cloud water, rain, cloud ice, snow, graupel (or hail), and chemical species.

The cloud microphysics is described by the single moment (bulk water) approach (Lin et al., 1983). Mass mixing ratios of cloud water, rain, ice, snow, and hail are predicted. Cloud water and ice are monodispersed and rain, snow, and hail have prescribed inverse exponential size distributions. For the simulations performed here, hail hydrometeor characteristics (ρ_h = 900 kg m^{-3}, N$_o$ = 4×10^4 m^{-4}) are used.

The gas-phase and aqueous chemistry (Barth et al., 2007) represent daytime chemistry of 15 chemical species, methane (CH_4), CO, O_3, hydroxyl radical (OH), hydroperoxy radical (HO_2), methylhydroperoxy radical (CH_3OO), NO_2, NO, HNO_3, H_2O_2, methyl hydrogen peroxide (CH_3OOH), CH_2O, formic acid (HCOOH), sulfur dioxide (SO_2), aerosol sulfate (SO_4), and ammonia (NH_3). Dissolution of soluble species is assumed to be in Henry's Law equilibrium for low solubility species (e.g. CO) or is treated as diffusion-limited mass transfer for high solubility species (Barth et al., 2001). When cloud water or rain freezes, the dissolved species is retained in the frozen hydrometeor. Adsorption of gases onto ice or snow was not included in the simulation. The acidity of the cloud water and rain drops are calculated separately based on a charge balance. The chemical mechanism is solved with an Euler backward iterative approximation using a Gauss-Seidel method with variable iterations. A convergence criterion of 0.01% is used for all the species.

The production of NO_x from lightning is the same as that in the UMd/GCE model

(see Sect. 3.3) which follows DeCaria et al. (2005). The parameterization uses observed National Lightning Detection Network (NLDN) and lightning interferometer data to determine when a lightning flash occurs and whether that flash is a cloud-to-ground (CG) stroke or an intracloud (IC) stroke. Lightning NO is distributed vertically either as a Gaussian distribution peaking in the mid-troposphere (CG flashes) or as a bimodal distribution peaking in the upper troposphere and mid-troposphere (IC flashes). At each model level, NO is divided equally among all grid cells within the 20 dBZ region of the storm.

The model is configured to a $160\times160\times20\,km^3$ domain with 161 grid points in each horizontal direction (1 km resolution) and 51 grid points in the vertical direction with a variable resolution beginning at 50 m at the surface and stretching to 1200 m at the top of the domain. The simulation was integrated at a 10 s time step. To keep the convection near the center of the model domain, the grid is moved at $1.5\,m\,s^{-1}$ eastward and $5.5\,m\,s^{-1}$ southward.

3.2 Chien Wang's convective cloud model with chemistry (C. Wang)

The convective cloud model of Wang and Chang (1993a) coupled with chemistry solves the 3-D pseudo-elastic form of the continuity equation. The thermodynamic equations use an ice-liquid potential temperature as a conserved variable (Tripoli and Cotton, 1981). A δ four-stream radiation code Fu and Liou (1993), with predicted O_3, water vapor, and liquid and ice phase hydrometeors, is used to compute the radiation transfer at both short and long waves (Wang and Prinn, 2000). The advection of the chemical species including aerosols is calculated by using a revised Bott scheme (Bott, 1989, 1993) by Wang and Chang (1993a).

The cloud microphysics module predicts both number concentration and mass mixing ratios of cloud particles (e.g., a 2-moment scheme; Wang and Chang, 1993a). Two liquid and two ice phase hydrometeors are represented in the model version for this intercomparison. The precipitating ice hydrometeor has graupel-like characteristics. The aerosol module used for the current simulations has a prognostic CCN (hygroscopic)

and IN (insoluble) calculation (Wang and Prinn, 2000). The CCN and IN calculations include transport, nucleation, and precipitation scavenging. The initial surface number concentration of CCN and IN is set to be 500 cm^{-3} and 100 L^{-1}, respectively. Note that the actual nucleation rate of aerosols is determined by both the availability of aerosols and temperature as well as supersaturation at the grid point (Wang, 2005a).

The chemistry sub-model predicts atmospheric concentrations of 25 gaseous and 8 aqueous chemical species (in both cloud droplets and raindrops and thus 16 prognostic variables), undergoing more than 100 reactions of NO_x-HO_x-O_3-CO-CH_4-Sulfur chemistry as well as transport and microphysical conversions (Wang and Chang, 1993a; Wang et al., 1998a; Wang and Prinn, 2000). Dissolution of soluble species is parameterized via diffusion-limited mass transfer. When freezing of liquid hydrometeors occurs, the dissolved gases are assumed to be retained in the frozen hydrometeors. The chemistry mechanism is solved with the Livermore solver for ordinary differential equations (LSODE) (Hindmarsh, 1983; Wang et al., 1998a). A module of heterogeneous uptake by ice particles of several key chemical species including O_3, H_2O_2, HNO_3, CH_2O, CH_3OOH, SO_2, and H_2SO_4 based on the first-order reaction approximation is also included (Wang, 2005b).

The production of NO_x from lightning follows the disk model of Wang and Prinn (2000). The lightning rate is derived as a parameterization of actually predicted collision rate between ice crystals and graupel as well as dynamic variables by the model. A prescribed CG/IC ratio (not predicted by the parameterization) of 5% is adopted based on the observation. NO production is set to be 465 moles NO per flash for both IC and CG flash. The freshly-produced NO molecules are distributed vertically based on either two (IC) normal distributions centered respectively at ice crystal and graupel concentrated layers or one (CG) such distribution centered at the latter layer, generally following DeCaria et al. (2000).

The model domain is 145×120 km^2 horizontally with a 1 km spatial resolution. The model domain extends from the surface to 20 km with a uniform grid spacing of 400 m. The time step for the 3 h integration is 3 s.

3.3 UMd/GCE (K. Pickering, L. Ott, G. Stenchikov)

The UMd/GCE modeling system consists of the 3-D Goddard Cumulus Ensemble (GCE) model (Tao and Simpson, 1993; Tao et al., 2001) and the University of Maryland offline cloud-scale chemical transport model (CSCTM; DeCaria et al., 2005). The output of the GCE model is used to drive the CSCTM.

The GCE model hydrodynamics is based on a complete set of compressible, nonhydrostatic equations in a Cartesian coordinate system. A second order finitedifference scheme in the vertical direction and the positive definite non-oscillatory horizontal advection scheme with small implicit diffusion (Smolarkiewicz, 1984; Smolarkiewicz and Grabowski, 1990) are employed. Open boundary conditions of Klemp and Wilhelmson (1978b) are used at the lateral boundaries. Newtonian damping is applied to the potential temperature and components of horizontal velocity at the top of the domain at about 25 km. A parameterization of sub-grid turbulent mixing is based on the prognostic equation for turbulent kinetic energy (Deardorf, 1975; Klemp and Wilhelmson, 1978a, b; Soong and Ogura, 1980). Turbulent mixing is handled in the cloud model using a turbulent diffusion approximation.

To parameterize cloud microphysics a Kessler-type scheme (Kessler, 1969; Houze, 1993) for liquid hydrometeors (cloud water and rain) and the three-category scheme of Lin et al. (1983) for solid hydrometeors (ice, snow, and hail) are employed. The hydrometeors are assumed to be spherical with exponential size distributions except for cloud water and cloud ice, which are monodisperse. Hail characteristics are used for the simulation.

Output from the 3-D GCE model simulation was used to drive a 3-D Cloud-Scale Chemical Transport Model (CSCTM, DeCaria et al., 2005). Temperature, density, wind, hydrometeor (rain, snow, graupel/hail, cloud water, and cloud ice), and diffusion coefficient fields from the GCE model simulation are read into the CSCTM every ten minutes, and these fields are then interpolated to the model time step of 15 s. The transport of chemical species is calculated using a van Leer advection scheme (Allen et al., 1991).

ACPD
7, 8035–8085, 2007

The lightning NO scheme in the CSCTM, described fully in DeCaria et al. (2005), is based on observed flash rate data. CG flash rates were calculated from NLDN observations and IC flash rates were determined by subtracting CG flash rates from total lightning flash rates obtained from interferometer observations. NO from CG flashes is distributed according to a Gaussian distribution peaking in the mid-troposphere while NO from IC flashes is distributed bimodally based on the typical vertical distributions of the VHF sources of IC and CG flashes from MacGorman and Rust (1998). NO from both types of flashes is also distributed vertically proportional to pressure. In each model layer, lightning NO is horizontally distributed uniformly to all grid cells with computed radar reflectivity greater than 20 dBZ. Production per CG flash (PCG) was estimated to be 390 mol NO per flash based on the mean peak current of CG flashes observed by the NLDN and a relationship between peak current and energy dissipated (Price et al., 1997). An estimate of NO production per IC flash (PIC) was obtained by assuming various PIC/PCG ratios and comparing the results with anvil aircraft measurements. Assuming a PIC/PCG ratio of 0.5 produced a favorable comparison with observed in cloud NO_x mixing ratios and as a result, PIC was estimated to be 195 moles NO per flash.

The CSCTM combines transport and lightning production with a chemical solver (SMVGEAR-II, Jacobson, 1995) and photochemical mechanism to simulate the chemical environment within the storm. The reaction scheme focuses on ozone photochemistry, containing the nonmethane hydrocarbons ethane, ethene, propane, and butane as described in DeCaria et al. (2000, 2005). The chemical scheme involves 35 active chemical species, 76 gas phase chemical reactions, and 18 photolytic reactions. Soluble species are removed from the gas phase by cloud and rain water with a dependence on Henry's Law coefficients. Uptake by ice is not included. Aqueous and multiphase reactions are not included. Photolysis rates are calculated as a function of time and are perturbed by the cloud, using typical summertime estimates from Madronich (1987) and cloud thickness taken from the GCE model output. Initial condition profiles of PAN, ethane, ethene, propane, and butane were taken from profiles constructed

using observations from the 12 July STERAO storm by DeCaria et al. (2005). The single column "spin-up" version of the CSCTM was run for 15 min to allow the chemical concentrations to come into equilibrium before starting the simulation of the storm.

The UMd/GCE modeling system was integrated in a domain of $360 \times 328 \times 25\,km^3$ in the x, y and z directions, respectively. The horizontal grid spacing was 2 km in both horizontal directions, and 0.5 km in the vertical. The GCE meteorology model was integrated using a 3 s time step to maintain numerically stability. The chemistry transport model is updated with a 30 s time step (though SMVGEAR-II itself uses a smaller time step based on stiffness).

3.4 RAMS (M. Leriche and S. Cautenet)

Gas and aqueous chemistry have been incorporated into the RAMS version 4.3 (Cotton et al., 2003). The basic equations in RAMS for solving the dynamical and thermodynamical variables are non-hydrostatic time-split compressible. The available options in the model include resolution ranging from few meters to a hundred kilometers, domains from a few kilometers to the entire globe and a suite of physical options for turbulence closure, cloud microphysics, radiation, lower boundary (soil/vegetation/snow and ocean surface), upper and lateral boundary conditions. RAMS has a multiple grid nesting scheme leading to solve the model equations simultaneously on any number of meshes.

The cloud microphysics module predicts both number concentration and mass mixing ratios of cloud particles, i.e. a two-moment bulk scheme (Meyers et al., 1997), using gamma distributions to represent the hydrometeor size distributions. For the simulation performed here, the water categories include cloud and rain drops and three ice condensate species: pristine ice, snow, and hail.

The chemistry module includes both gas and aqueous phase chemistry. For gas-phase chemistry, the mechanism includes 29 species and describes the reactivity of ozone, NO_y and VOC including isoprene chemistry (Arteta et al., 2006; Taghavi et al., 2004). For aqueous-phase chemistry, the mechanism includes 10 species and

represents the HO_x chemistry and the formation of nitrate, sulfate and formic acid (Audiffren et al., 2004). For the exchange of chemical species between gas phase and liquid hydrometeors, the mass transfer kinetic formulation of Schwartz (1986) is used taking into account the possible deviation from Henry's law equilibrium. The redistribution of chemical species by microphysical processes is only considered for liquid hydrometeors. Therefore, when freezing of liquid water occurs, the dissolved species are degassed. The interactions of chemical species with ice phase are not yet implemented in the model.

The lightning-NO_x parameterization is based on Pickering et al. (1998). The parameterization consists of four parts: flash rate, flash type, flash location and NO production rate. The flash rate is computed from the maximum vertical velocity using a power law. The fractions of intracloud (IC) and cloud to ground (CG) flash are computed by estimating the depth of the layer from the freezing level (the 0°C isotherm in the cloud) to the cloud top. The CG flashes are placed within the 20 dBZ region from the surface to the model-calculated –15°C isotherm and the IC flashes in the region of the cloud above the –15°C isotherm. The NO production rate is then calculated for each CG and IC flash using different rate values for CG and IC flashes.

For the simulation of the STERAO storm, two nesting grids are used, the large one of 240×240×20 km^3 with a horizontal resolution of 3 km and the small one of 120×120×20 km^3 with a horizontal resolution of 1 km. The small grid moves into the large one with a constant velocity of 1.5 $m\,s^{-1}$ towards the east and 5.5 $m\,s^{-1}$ southward. A 5 s time step is used.

3.5 Meso-NH (J.-P. Pinty, C. Barthe, and C. Mari)

The Meso-NH model integrates an anelastic system of equations. The model can be used to simulate real cases (starting from ECMWF analyses) or ideal cases (the STERAO case for instance). The model is fully explicit. It contains all the necessary parameterizations to run a meteorological case. Grid nesting is available with 1 or 2-way coupling. In addition, the model contains a flexible chemical scheme, an aerosol

scheme, a 1- or 2-moment microphysical scheme and an electrical scheme.

The Multidimensional Positive Definite Advection Transport Algorithm (MPDATA) is used for the advection scheme, and turbulence is parameterized with a 3-D scheme. In addition, a gravity wave damping layer is placed between the model top and 15 km height.

The cloud microphysics is described by a mixed-phase scheme (Pinty and Jabouille, 1998) that takes into account 6 water variables (water vapor, cloud droplets, raindrops, pristine ice, snow and graupel). For this study, graupel-like characteristics are used. Only mass mixing ratios of these microphysical species are predicted. Meso-NH also contains an explicit electrification and lightning flash scheme (Barthe et al., 2005). The electric charges are carried by each of the hydrometeor categories and are separated via non-inductive processes (i.e., ice-graupel collisions). Lightning flashes are triggered when the ambient electric field exceeds a threshold ($167\rho(z)$ kV m^{-1}). The lightning flashes produce both bi-directional leaders and branch streamers (Barthe et al., 2005). Nitrogen oxides are added along the lightning flash path as a function of the pressure and the channel length as suggested by Wang et al. (1998b) from laboratory experiments (Barthe et al., 2007).

For these simulations, only the scavenging of the soluble gases, CH_2O, H_2O_2, and HNO_3 are considered. The partitioning between gas and liquid phases is calculated following the mass transfer kinetic formalism of Schwartz (1986). These species do not react chemically. The scavenged gases are tracked in the cloud droplets and in the rain drops only, but not in the ice phase. Note that the liquid drops do get transported to the glaciated regions of the modeled storm. CO and O_3 are insoluble. NO_x is represented by 2 variables: the first one corresponds to the background NO_x and the second one includes both background and the NO_x produced from lightning.

The simulation is configured to that described by Skamarock et al. (2000). The computational domain is 160×160×50 grid points with a horizontal resolution of 1 km and a vertical spacing ranging from 75 m at the ground to 700 m in the stratosphere. The time step (2 s) is low to get an accurate transport of the trace gases.

ACPD
7, 8035–8085, 2007

3.6 SDMST (John Helsdon, Richard Farley)

The 3D SEM (Storm Electrification Model) has fully coupled microphysical, electrical and chemical processes. The model is a modified form of the 3-D nested grid model developed by Terry Clark and associates (Clark, 1977; Clark, 1979; Clark and Farley, 1984; Clark and Hall, 1991). The model is nonhydrostatic and uses the anelastic approximation to eliminate sound waves. For the dynamics, the model employs the flux form of the second-order operators of Arakawa (1966) for the spatial derivatives, and treats time derivatives using a second-order leapfrog scheme. This formulation allows the model to conserve kinetic energy. Advection of scalar quantities uses the multidimensional positive-definite advection transport algorithm (MPDATA) developed by Smolarkiewicz (1984) and Smolarkiewicz and Clark (1986). Subgrid-scale turbulence is parameterized according to first-order theory.

The model employs the single moment (mixing ratio) microphysical parameterization scheme of Lin et al. (1983) which allows five hydrometeor classes; cloud water, rain, cloud ice, snow, and graupel/hail. For the simulation reported here, the model uses parameters characteristic of hail to represent the graupel/hail field. The treatment of electrical processes follows Helsdon and Farley (1987) and Helsdon et al. (2001). Each hydrometeor class has an associated charge density in addition to the positive and negative small ion concentrations that combine to form the total charge density, which is related to the electrical potential through Poisson's equation. Gas phase chemical processes are included in the model as described in Zhang et al. (2003). This formulation allows 18 reactions involving nine tracked chemical species which include NO, NO_2, O_3, CH_4, CO, OH and HO_2, with HNO_3 as a sink.

The simulation includes an explicit prediction of intracloud lightning discharges as described in Helsdon et al. (1992) and Helsdon et al. (2002). A lightning channel is initiated when and where a threshold electric field is attained (225 kV m^{-1} in this case) and propagates bi-directionally away from the initiation point following the electric field vector. The channel terminates when the electric field at the ends of the propagating

channel drops below a preset value (75 kV m^{-1}). Once the channel is formed, its linear charge density is calculated from theory and converted into an equivalent small ion density. The charged channel modifies the electric field and consequently modifies the electric energy in the domain in a physically consistent manner. By calculating the electrical energy just before and immediately after the discharge, the energy dissipation can be determined. NO production (9×10^{16} NO molecules J^{-1} at sea level) is proportional to this electrical energy change and pressure, and is limited to the immediate vicinity of the lightning channel.

The simulation is configured to a $120\times120\times20$ km^3 domain using 1 km horizontal grid spacing and 250 m vertical resolution. The model integrations employed a 2-s time step. A Galilean transformation is applied to keep the main convection within the interior regions of the domain. For the 10 July STERAO case the grid translates to the east at 4 m s^{-1} and to the south at 5 m s^{-1}.

3.7 DHARMA (A. Fridlind, A. Ackerman)

The DHARMA (Distributed Hydrodynamic Aerosol-Radiation-Microphysics Application) model treats atmospheric and cloud dynamics with a large-eddy simulation code (Stevens and Bretherton, 1996) that solves an anelastic approximation of the Navier-Stokes equations appropriate for deep convection (Lipps and Hemler, 1986).

Embedded within the dynamics code, DHARMA treats aerosol and cloud microphysics with the CARMA (Community Aerosol-Radiation Model for Atmospheres) code (Ackerman et al., 1995; Jensen et al., 1998). Aerosols, water drops, ice crystals, and solute within the drops and crystals are tracked in a range of sizes (16 size categories each). The density of ice is a function of size, roughly representative of conical graupel. Microphysical processes include aerosol activation into drops, condensational growth and evaporation of drops, gravitational collection, spontaneous and collision-induced drop breakup, homogeneous and heterogeneous freezing of aerosols and drops, depositional growth and sublimation of ice, sedimentation of liquid and ice, melting, and

Hallett-Mossop rime splintering. The microphysics treatment is identical to that used by Fridlind et al. (2005), where further detail is provided.

The DHARMA model only transports trace gases. Chemistry and production of NO_x from lightning are not included in the model.

Results shown here are for uniform 1 km horizontal resolution and 250 m vertical resolution over a $120 \times 120 \times 20\ km^3$ domain, which is nudged to the initial profile along each face. Dynamics and gravitational collection are advanced with a 5-s time step; all other microphysical processes are advanced with a time step of 0.2 to 5 s that is chosen based on the processes that are active in each grid cell as the simulation progresses.

3.8 Vlado Spiridonov's convective cloud model with chemistry (Vlado Spiridonov, Bosko Telenta)

The model (Spiridonov and Curic, 2003, 2005) is a three-dimensional, non-hydrostatic, time-dependant, compressible system using the dynamic and thermodynamics schemes from Klemp and Wilhelmson (1978a) and the bulk cloud microphysics scheme from Lin et al. (1983) that takes into account 6 water variables (water vapor, cloud droplets, ice crystals, rain, snow, and graupel). The graupel hydrometeor class is represented as hail with a density of $0.9\ g\ cm^{-3}$. The chemistry module includes sulfate chemistry (Taylor, 1989) both inside and outside clouds. The absorption of chemical species from the gas phase into cloud water and rainwater is determined by either Henry's law equilibrium (Taylor, 1989), or by diffusion-limited mass transfer between gas and liquid phases to include possible non-equilibrium states, (Barth et al., 2001). All equilibrium constants and oxidation reactions are temperature dependent according to the van't-Hoff relation (Seinfeld, 1986). Cloud water and rainwater pH is calculated using the charge balance equation from Taylor (1989). The model includes a freezing transport mechanism of chemical species based on Rutledge et al. (1986). Thus, when water from one hydrometeor class is transferred to another, the dissolved scalar is transferred to the destination hydrometeor in proportion to the water mass that was transferred. Production of NO from lightning is not parameterized in the Spiridonov

model.

For the intercomparison simulation, the model is configured to a domain of $140 \times 140 \times 15\,km^3$ with 1 km horizontal resolution and 500 m vertical resolution. A 10 s time step is used for the integration.

4 Results

Four types of model results are presented. First, the storm intensity and structure are analyzed by intercomparison of peak vertical velocity and radar reflectivity with observations. Second, the redistribution of CO, O_3 and NO_x are presented, and anvil mixing ratios are compared with analyzed UND Citation aircraft measurements. Then the flux of air, CO and NO_x through a plane across the anvil is compared to that determined from the observations. Lastly the mixing ratios of CH_2O, H_2O_2, and HNO_3 in the anvil are compared among models.

4.1 Storm intensity and structure

The maximum vertical velocity in the model domain was recorded at 10-minute intervals (Fig. 2). Each model shows a rapid increase in peak updraft velocity at the beginning of the simulation. Most simulations maintain peak updrafts above $24\,m\,s^{-1}$ during the remainder of the simulation, while radar observations show peak updrafts to be between 24 and $38\,m\,s^{-1}$. Transitions to updraft velocities of $35\,m\,s^{-1}$ or more are seen by C. Wang's model, WRF-Aqchem, DHARMA, and Meso-NH. The height of the peak updraft ranges from 7 km to 14 km m.s.l., which is similar but somewhat higher than observations.

The storm structure can be evaluated by comparing the modeled radar reflectivity to the observed radar reflectivity. Both horizontal and vertical cross-sections of radar reflectivity are examined. At 23:12 UTC 10 July, the CSU CHILL radar reflectivity at z = 10.5 km m.s.l. indicates two convective cores oriented in a northwest-southeast

ACPD
7, 8035–8085, 2007

line with an anvil spreading to the east-southeast (Fig. 3). After 1 h of simulation, the results from the models have 2–3 convective cores oriented northwest-southeast. The magnitude of the reflectivity differs among models due to 1) whether graupel characteristics (C. Wang, Meso-NH, DHARMA models) or hail characteristics are modeled, 2) horizontal resolution, and 3) single-moment versus multi-moment (C. Wang, DHARMA, RAMS models) microphysics parameterizations. The width of the anvil varies among models. The observed reflectivity has an anvil width of 32–40 km at 23:12 UTC, while model results range from 12.5 km to 45 km. Seifert and Weisman (2005) noted that double-moment microphysics parameterizations tend to produce broader anvils than single-moment microphysics parameterizations. The results from our study do not distinctly show this correlation. While C. Wang's model with double-moment microphysics has a widespread anvil, DHARMA and RAMS have anvils similar in width to the models with single-moment microphysics. Other factors contributing to the anvil width are the graupel or hail characteristics used (which influences the particle's fall speed), the dynamics formulation, and the horizontal resolution.

The vertical cross section of observed reflectivity along the storm axis (Fig. 4) shows that the northwest core (left side of figure) is decaying while the southeast core is reaching its mature stage. During the multicell stage of the storm, radar reflectivity plots show 2 to 4 convective cores being active at any given time. All of the models show 3 convective cores, with all cores of approximately the same reflectivity magnitude except for the Meso-NH model. The Meso-NH model has weaker reflectivity most likely because of the graupel (rather than hail) characteristics used in their microphysics parameterization. While the reflectivity in the observed anvil is weak (5–20 dBZ) and somewhat extensive (>35 km from the southeast core to the anvil edge), the simulated anvils are stronger (5–35 dBZ) and less extensive (15–25 km from the southeast core to the anvil edge). The maximum height of the modeled reflectivity varies among models. The reflectivity simulated by Spiridonov only reaches 11.5 km m.s.l., while the reflectivity simulated by the C. Wang and RAMS models reach 16.5 km m.s.l. Observations show the reflectivity top to be 14.5 to 16.5 km m.s.l.

ACPD
7, 8035–8085, 2007

EGU

In summary, the discrepancies among models for radar reflectivity, which are mainly due to the differences between the treatments of cloud microphysics, highlight the difficulty of modeling the realistic structure of clouds even using cloud resolving models. Nevertheless, the modeled cloud structures are all reasonably simulated. Thus, it is possible to use these models to simulate trace gas transport as part of the intercomparison.

4.2 Distributions of CO, O_3, and NO_x

Mixing ratios of CO, O_3, and NO_x are compared to observations using two approaches. First, model results are evaluated with aircraft measurements which were obtained from the University of North Dakota (UND) Citation aircraft as it flew across the anvil. Second, cross-sections of the mixing ratios are compared to a derived cross-section obtained from several transects of the anvil by the aircraft.

The UND Citation aircraft sampled the outflow region of the storm by performing across-anvil transects at different levels in the anvil (transects indicated in Fig. 3). Two transects are used to compare model results with observations. The first transect is 10 km downwind of the southeastern-most convective cell at 23:10 UTC (which corresponds to t = 1 h in the simulations) at 11.6 km m.s.l. The second transect is ~50 km downwind of the southeastern-most convective cell at 23:35 UTC (corresponding to t = 1 h 30 min in the simulations) at 11.2 km m.s.l.

Mixing ratios of CO in the anvil are observed to be enhanced compared to the background upper troposphere (Fig. 5) because convective transport moves high mixing ratios from the boundary layer to the upper troposphere. Conversely, O_3 mixing ratios are lower in the anvil than in the upper troposphere because relatively-low O_3 mixing ratios are transported from the boundary layer. The model simulations predict these enhancements and depletions of CO and O_3 mixing ratios, which agree with the observations (Fig. 5), especially in the core of the anvil. All models underpredict the O_3 mixing ratio on the southwest edge of the anvil, a feature that may be attributed to mixing of stratospheric air as is discussed below. Nevertheless, all the models do a good

job transporting these passive tracers within the anvil.

Observed NO mixing ratios (Fig. 6) are strongly enhanced within the anvil compared to the background upper troposphere primarily due to lightning production of NO. Modeled NO_x mixing ratios show the importance of the lightning source. The DHARMA and Spiridonov models do not include production of NO_x from lightning and therefore substantially underpredict the NO_x mixing ratios. The other models, which include lightning-produced NO_x, generally show NO_x mixing ratios elevated compared to the DHARMA and Spiridonov models within the anvil. For the first transect, WRF-AqChem, C. Wang, Meso-NH, and SDSMT NO_x mixing ratios are similar to the observations, but for shorter across-anvil distances. Only the Meso-NH model has a similar area under the curve as the observations, indicating the total amount of NO_x placed into the 11.8 km m.s.l. height is realistic (note that mass fluxes of NO_x integrated over the across-anvil area and over time are discussed in the next section). For the second transect, all of the models that include NO_x production by lightning agree reasonably well with observations. This is the first time simulated lightning NO_x production from a specific model transect has been directly compared with observations from the corresponding specific aircraft transect of a storm anvil. To obtain NO_x mixing ratios similar in magnitude to observations is encouraging and indicates that model parameterizations are capturing the key parameters of lightning NO_x production.

Skamarock et al. (2003) analyzed the UND Citation aircraft data taken across the anvil of the storm. The Citation aircraft mapped out the anvil structure during ~1 h 30 min time period by traversing the anvil in horizontal passes, approximately perpendicular to the long axis of the anvil, at elevations starting at approximately 11.8 km m.s.l. (close to the anvil top) and ending at approximately 6.8 km m.s.l. Skamarock et al. (2003) projected the cloud particle concentration, CO, O_3, and NO observations onto a vertical plane using an objective analysis procedure. Model predictions of these variables taken along a similar plane (similar to the T2 cross-section shown for WRF-AqChem in Fig. 3) can then be compared to the analyzed observations.

Vertical cross-sections across the anvil of cloud particle concentration are shown in

Fig. 7. The analyzed observations are for ice >25 μm diameter (D_{ice}) based on the measurements from the Particle Measuring Systems 2-D probe (Dye et al., 2000). The results from the models tend to match or over-predict the observations. The results from the C. Wang and RAMS models are only for D_{ice}>25 μm giving good agreement with observations. While the DHARMA results are also only for ice with D_{ice} >25 μm, the results overpredict the ice particle number, suggesting other factors contribute to increased predicted ice particle number. Using graupel characteristics instead of hail can also increase ice concentrations in the anvil region because graupel has a smaller fall speed and therefore is carried further into the anvil. The models that predicted only the mass of the cloud particles (WRF-AqChem, UMd/GCE, Meso-NH, SDSMT, Spiridonov) assumed a diameter for the ice hydrometeor category (for example, WRF-AqChem set D_{ice}=45 μm) for the purposes of estimating the number concentration. The calculation of number concentration is very dependent on the assumed ice diameter since the anvil is primarily composed of small ice particles.

Carbon monoxide mixing ratios analyzed from the observations (Fig. 8) reach 110 nmol mol^{-1} or so in the anvil. Simulated CO mixing ratios also reach those values in the anvil. There is a slight underprediction of CO seen in the WRF-AqChem model. In general, the models reasonably simulate CO mixing ratios in the anvil.

Vertical cross-sections of observed O_3 (Fig. 9) show O_3 being depleted in the anvil to values of about 80–100 nmol mol^{-1}, but also show a small region of downward-intruding, high (>300 nmol mol^{-1}) O_3 at the top of the anvil on the SSW edge (upper left part of figure). The C. Wang and RAMS models also show some downward intrusion of O_3 on the SSW upper edge of the anvil (note the change in vertical gradient of O_3 at z = 13.5 km m.s.l. on the left side of the anvil) or upward intrusion of low O_3 at the top of the convective cores, but none of the other models reproduce the change in the O_3 vertical gradient. Both the C. Wang and RAMS models have tall convective cores at t = 1 h (Fig. 4), thus the vertical extent of the updraft in connection with turbulent mixing at the tropopause may be responsible for the high O_3 at the top of the anvil on the SSW edge. In agreement with observations, all the models show mixing ratios of

80 nmol mol^{-1} in the anvil.

The analyzed NO mixing ratios from observations have peaks of NO of over 500 pmol mol^{-1} (Fig. 10) within a broad region of NO >200 pmol mol^{-1}. Note that the observations are of NO while the model results are of NO_x. By assuming photochemical equilibrium between NO and NO_2, NO_x mixing ratios are approximately 30% greater than NO mixing ratios (Skamarock et al., 2003). Thus, modeled NO_x should be ~30% greater than the observed NO. Results from models that did not include production of NO_x from lightning (DHARMA, Spiridonov) do not predict the NO_x>500 pmol mol^{-1} peaks, but instead show NO_x~200 pmol mol^{-1} in the anvil; much less than that observed. The models with production of NO_x from lightning (WRF-AqChem, C. Wang, UMd/GCE, RAMS, Meso-NH and SDSMT) do predict peaks of NO_x on the same order of magnitude as the observations. These models also have a broad region of NO_x mixing ratios between 150 and 250 pmol mol^{-1}, similar to those seen in the observations. To obtain the observed peak values of the NO_x, production from lightning must be modeled.

4.3 Mass fluxes in the anvil outflow

Utilizing the modeled mixing ratio of (C) in the anvil cross-sections (shown in Figs. 8–10) and the horizontal velocity ($U\perp$) perpendicular to the cross-section plane, estimates of mass fluxes can be made. Corresponding mass fluxes of air, CO, and NO_x are derived from the aircraft measurements (Skamarock et al., 2003) for comparison to the model results. The calculation of the modeled mass flux density is

$$\text{flux} = \frac{\sum_{\text{anvil cells}} \rho\, U\perp\, C\, \Delta\ell\, \Delta z}{\sum_{\text{anvil cells}} \Delta\ell\, \Delta z}$$

where $\Delta\ell$ and Δz are the horizontal and vertical grid cell spacing within the anvil. The flux density is determined only in the region where cloud particles exist in the anvil.

Table 3 lists the anvil area as well as the fluxes of air mass, CO, and NO_x averaged over a 1 h time period, which is comparable to the time period of the aircraft measurements. Each model's average mass flux can be compared to the mass flux derived from observations, which was determined by Skamarock et al. (2003) from the analyzed cross section.

While the analyzed anvil area taken from the observations is 315 km^2, the modeled anvil area ranges from 109 km^2 to 590 km^2, which are within –65 and 90% of the analyzed observed area. The air mass flux determined from the observations is 5.9 $kg\,m^{-2}\,s^{-1}$, while that predicted by the models ranges from 6.6 to 9.1 $kg\,m^{-2}\,s^{-1}$. Note that there is also some uncertainty in the observed anvil area and flux densities (Skamarock et al., 2003) associated with uncertainties in the in situ measurements and in temporal changes in these measured species and in the anvil cross-section area as the measurements were taken. All of the models overpredict the air mass flux, suggesting that the modeled wind speeds in the anvil are too strong. The CO flux density calculation from the observational analysis is 1.9×10^{-5} moles $m^{-2}\,s^{-1}$, while the modeled CO flux densities range from 1.93 to 2.8×10^{-5} moles $m^{-2}\,s^{-1}$. We find that 4 models are within 5% of the analyzed CO flux density and a total of 7 models are within 33%. However, because the air mass flux is over-predicted by these same models, a correction to the air mass flux density would result in CO flux densities being smaller than the analysis of the measurements. The NO_x flux density derived from the observations includes NO_x produced from lightning and has a value of 5.8×10^{-8} moles $m^{-2}\,s^{-1}$. The NO_x flux densities determined from models without lightning-NO_x production (DHARMA, Spiridonov) are 4.3×10^{-8} and 2.7×10^{-8} moles $m^{-2}\,s^{-1}$, while the models that do include lightning-NO_x production are between 3.9 and 13.0×10^{-8} moles $m^{-2}\,s^{-1}$. We find that the variability among the modeled NO_x flux densities is clearly higher than that for the air mass or CO flux densities.

ACPD
7, 8035–8085, 2007

EGU

4.4 Distributions of CH_2O, H_2O_2, and HNO_3

Soluble and reactive chemical species, such as formaldehyde, hydrogen peroxide and nitric acid, are important to tropospheric ozone chemistry. In simulating CH_2O, H_2O_2, and HNO_3, species with different solubility coefficients and different chemical reactivity are represented. Because there were no observations of CH_2O, H_2O_2, and HNO_3 in the outflow region of the 10 July 1996 STERAO storm, comparisons to measurements are not possible. While other field campaigns have measured one or more of these species near convection, none of the campaigns have done a budget (detrained species in the anvil minus entrained species into the convective core) nor have the measurements been near the storm core as these model results are. These previous field campaigns have shown some enhancement of CH_2O and H_2O_2 and strong depletion of gas-phase HNO_3 in convective outflow regions compared to their background upper troposphere mixing ratios. Here, we compare gas-phase mixing ratios for these 3 species to find similarities and differences among model approaches. How the simulated results compare to past field campaigns is discussed at the end of the section.

The soluble, reactive species are simulated by 5 models: WRF-AqChem, C. Wang, UMd/GCE, RAMS, and Meso-NH. Model results along the same two aircraft transects are used for the comparison (Fig. 11). In contrast to the CO and O_3 results, the modeled CH_2O, H_2O_2, and HNO_3 gas-phase mixing ratios vary significantly among models. For CH_2O, the Meso-NH, RAMS, and UMd/GCE simulations have enhanced CH_2O mixing ratios compared to their values in the background upper troposphere. The WRF-AqChem and C. Wang simulations have anvil mixing ratios that are depleted or similar to the background upper troposphere mixing ratios. One explanation for the disagreement among model results is the manner in which soluble species are treated with the ice phase. The Meso-NH, RAMS, and UMd/GCE models do not include soluble species in the ice phase while WRF-AqChem and C. Wang models do. Both the WRF-AqChem and C. Wang models use a retention efficiency of 100% when cloud

and rain drops freeze. Thus, in these two models the CH_2O in the snow and hail is precipitated with their parent hydrometeor, transferred to the rain via melting, and rained onto the ground (Barth et al., 2001, 2007). The WRF-AqChem, degas curves in Fig. 11 illustrate the effect of not including soluble species in the ice phase. A second explanation for differences in CH_2O mixing ratios is the effect of chemistry. The Meso-NH model does not include gas or aqueous chemistry, while WRF-AqChem, C. Wang and RAMS do include gas-phase and aqueous chemistry, and UMd/GCE includes only gaseous chemistry. Previous studies (Leriche et al., 2007; Barth et al., 2007) showed that both gas-phase and aqueous chemistry (using a chemistry mechanism without non-methane hydrocarbons) reduce CH_2O mixing ratios in the anvil. Similarly the assumption of Henry's law equilibrium for gas-aqueous species transfer (UMd/GCE) could reduce gas-phase concentrations. Simulations without the production of NO from lightning performed by both the WRF-AqChem and C. Wang models show negligible differences from those shown in Fig. 11 for anvil CH_2O mixing ratios within 50 km of the storm core.

For H_2O_2, the UMd/GCE and RAMS model results have enhanced mixing ratios in the anvil compared to the background upper troposphere. The C. Wang and Meso-NH model results have similar mixing ratios between the anvil and background upper troposphere, while the WRF-AqChem model results have depleted H_2O_2 mixing ratios compared to the background upper troposphere. The effect of the ice phase (WRF-AqChem, degas curve) would enhance H_2O_2 mixing ratios in the anvil substantially. Lightning production of NO does not affect the results shown by the WRF-AqChem and C. Wang models. The inclusion of aqueous chemistry does reduce anvil mixing ratios of H_2O_2 somewhat (Leriche et al., 2007; Barth et al., 2007). Furthermore, the treatment of the gas-aqueous species transfer could affect results, with the assumption of Henry's law likely reducing gas-phase mixing ratios. Modified photolysis rates may increase H_2O_2 mixing ratios. The C. Wang and UMd/GCE models include cloud-modified photolysis reaction rates, while the other models do not. However, Barth et al. (2002) showed a very small effect of cloud-modified photolysis rates on H_2O_2 mixing

ratios in marine boundary layer clouds.

For HNO_3, all the models except the RAMS model has anvil mixing ratios that are depleted compared to the background upper troposphere. The C. Wang HNO_3 gas-phase mixing ratios go to zero in the anvil, while other models show values between 200 and 300 pmol mol^{-1}. The discrepancy is explained by adsorption of gas-phase HNO_3 onto ice and snow crystals which is included in the C. Wang model. When this process is not included (C. Wang, no ads curve), the HNO_3 mixing ratios in the anvil are similar to those predicted by the other models.

For soluble species, such as CH_2O, H_2O_2, and HNO_3, many processes affect their fate. Scavenging of these gases by the drops and ice tends to reduce their gas-phase mixing ratios in the anvil. Aqueous chemistry also tends to reduce mixing ratios of CH_2O and H_2O_2. Inclusion of dissolved species in the ice phase substantially reduces the gas-phase mixing ratios of CH_2O, H_2O_2, and HNO_3, but this is an uncertain result because of the uncertainties and lack of knowledge concerning the physical and chemical processes occurring when cloud and rain drops freeze. Production of NO by lightning does not affect the gas-phase mixing ratios of these species within 50 km of the storm core. Their mixing ratios may be affected further downwind as chemical aging occurs.

While measurements of formaldehyde, hydrogen peroxide, and nitric acid were not taken in the convective outflow of the 10 July 1996 STERAO storm, some of these species have been measured during other field campaigns near convection. Stickler et al. (2006) found enhanced upper troposphere CH_2O mixing ratios over Europe on a day influenced by convection compared to a day representative of background conditions. These measurements were taken well downwind of the convection therefore allowing chemical aging (i.e. production of CH_2O) to occur in the convective outflow plume. H_2O_2 measurements reported for tropical oceanic convection sampled in PEM Tropics A (Cohan et al., 1999) showed that H_2O_2 convective outflow mixing ratios were moderately enhanced (330±140 pmol mol^{-1}) compared to the unperturbed upper troposphere (200±110 pmol mol^{-1}). These results support the C. Wang results

ACPD
7, 8035–8085, 2007

(Fig. 11), but it must be recognized that the Cohan et al. measurements sampled tropical, oceanic convection (characterized by more liquid water and less ice) compared to the midlatitude, continental convection simulated in this study. Measurements of HNO_3 (Popp et al., 2004) revealed large depletions of gaseous HNO_3 in cirrus sampled during the CRYSTAL-FACE experiment in Florida. Their measurements are in agreement with the models showing gas-phase HNO_3 depleted mixing ratios (Fig. 11).

5 Conclusions

The intercomparison of convective scale cloud chemistry models simulating constituent transport in deep convection is the first of its kind. Simulations were performed based on the same initial conditions and similar model domain configurations. All eight models that participated in the intercomparison have reproduced the observed multicellular convection with radar reflectivity reaching >50 dBZ. Comparisons of carbon monoxide and ozone, which are primarily transported in convection, showed good agreement among models and with observations especially within the anvil. The models that included lightning production of nitric oxide predicted NO_x mixing ratios of similar magnitude to observed NO mixing ratios indicating that NO production from lightning is a key process to include for understanding the composition of convective outflow regions. Furthermore, the relatively good agreement with observations show that current cloud-scale parameterizations of lightning production of NO seem to be capturing the key parameters of this process. This is an important point because the parameterizations used ranged from physically-based NO production utilizing the explicit prediction of charge, to parameterizations based on peak updraft velocities, to those based on observed lightning flash input data.

Calculations of the anvil fluxes of air, CO and NO_x are compared between models and analyzed observations. The models consistently overestimate the flux density of air compared to the observed value, but flux densities of CO agree quite well with the observed value. The deviation among the models is 20% and less for the air and CO

flux densities. Predicted NO_x flux densities are significantly more variable and tend to be greater than that estimated from observations.

Formaldehyde, hydrogen peroxide, and nitric acid, species that are soluble and chemically reactive, are compared just among the different models because observations of these species were not made in the anvil region of the STERAO storm. For all 3 species, the models produced very different results indicating the need for measurements of these species in the anvil region to better understand their convective processing. Potential reasons for the discrepancies among the models include the role of the ice phase, the impact of cloud-modified photolysis rates on these species mixing ratios, and representation of their chemical reactivity.

To improve parameterizations of convective transport of constituents in large-scale models, we can use these models to obtain general characteristics (e.g. vertical mass fluxes and wet deposition rates) of chemical constituent transport in a variety of convection types. Further research needs to be conducted to understand what processes control the fate of the soluble species formaldehyde, hydrogen peroxide, and nitric acid. As part of this, measurements of these soluble, reactive species must concurrently be taken in both the inflow and outflow regions of a variety of convective storms.

Acknowledgements. The discussions and contributions of initial conditions and analyzed observations from W. Skamarock are greatly appreciated. More information on the intercomparison can be found at http://box.mmm.ucar.edu/people/barth/files/Chem_Convec_Intercomparison/tracertransportdeepconvection.html. Wiebke Deierling is thanked for providing the radar-derived maximum updraft speeds and heights. The University of Maryland/Rutgers investigators thank W.-K. Tao for use of the Goddard Cumulus Ensemble Model to drive the cloud chemistry calculations. The National Center for Atmospheric Research is operated by the University Corporation for Atmospheric Research under the sponsorship of the National Science Foundation.

References

Ackerman, A. S., Toon, O. B., and Hobbs, P. V.: A model for particle microphysics, turbulent mixing, and radiative-transfer in the stratocumulus-topped marine boundary-layer and comparisons with measurements, J. Atmos. Sci., 52, 1204–1236, 1995.

Allen, D. J., Douglass, A. R., and Rood, R. B.: Applications of a monotonic upstream transport scheme to three-dimensional constituent transport calculations, Mon. Weather Rev., 119, 2456–2464, 1991.

Arakawa, A.: Computational design for long term integration of the equations of motion: two-dimensional incompressible flow, J. Comput. Phys., 1, 119–143, 1966.

Arteta, J., Cautenet, S., Taghavi, M., and Audiffren, N.: Impact of two chemistry mechanisms fully coupled with mesoscale model on the atmospheric pollutants distribution. Atmos. Environ., 40, 7983–8001, 2006.

Audiffren, N., Buisson, E., Cautenet, S., and Chaumerliac, N.: Photolytic impact of a stratocumulus cloud layer upon the chemistry of an offshore advected plume of pollutants during the NARE 1993 intensive experiment: a numerical study, Atmos. Res., 70, 89–108, 2004.

Barth, M. C., Stuart, A. L., and Skamarock, W. C.: Numerical simulations of the July 10 STERAO/Deep Convection storm: Redistribution of soluble tracers, J. Geophys. Res., 106, 12 381–12 400, 2001.

Barth, M. C., Hess, P. G., and Madronich, S.: Effect of marine boundary layer clouds on tropospheric chemistry as analyzed in a regional chemistry transport model, J. Geophys. Res., 107, doi:10.1029/2001JD000468, 2002

Barth, M. C., Kim, S.-W., Skamarock, W. C., Stuart, A. L., Pickering, K. E., and Ott, L. E.: Simulations of the redistribution of formaldehyde, formic acid, and peroxides in the July 10, 1996 STERAO deep convection storm, J. Geophys. Res., in press, 2007.

Barthe, C., Molinie, G., and Pinty, J.-P.: Description and first results of an explicit electrical scheme in a 3D cloud resolving model, Atmos. Res., 76, 95–113, 2005.

Barthe, C., Pinty, J.-P., and Mari, C.: Lightning-produced NO_x in an explicit electrical scheme tested in a Stratosphere-Troposphere Experiment: Radiation, Aerosols, and Ozone case study, J. Geophys. Res., 112, D04302, doi:10.1029/2006JD007402, 2007.

Bott, A.: A positive definite advection scheme obtained by nonlinear renormalization of the advective fluxes, Mon. Weather Rev., 117, 1006–1015, 1989.

Bott, A.: The monotone area-preserving flux-form advection algorithm: Reducing the time-

splitting error in two-dimensional flow fields, Mon. Weather Rev., 121, 2637–2641, 1993.
Clark, T. L.: A small-scale dynamic model using a terrain-following coordinate transformation, J. Comput. Phys., 24, 186–215, 1977.
Clark, T. L.: Numerical simulations with a three-dimensional cloud model: lateral boundary condition experiments and multicellular severe storm simulations, J. Atmos. Sci., 36, 2191–2215, 1979.
Clark, T. L. and Farley, R. D.: Severe downslope windstorm calculations in two and three spatial dimensions using anelastic interactive grid nesting: a possible mechanism for gustiness, J. Atmos. Sci., 41, 329–350, 1984.
Clark, T. L. and Hall, W. D.: Multi-domain simulations of the time dependent Navier Stokes equation: benchmark error analyses of nesting procedures, J. Comp Phys., 92, 456–481, 1991.
Cohan, D. S., Schultz, M. G., Jacob, D. J., Heikes, B. G., and Blake, D. R.: Convective injection and photochemical decay of peroxides in the tropical upper troposphere: Methyl iodide as a tracer of marine convection, J. Geophys. Res., 104, 5717–5724, 1999.
Cotton, W. R., Pielke Sr., R. A., Walko, R. L, Liston, G. E., Tremback, C. J., Jiang, H., McAnelly, R. L., Harrington, J. Y., Nicholls, M. E., Carrio, G. G., and McFadden, J. P.: RAMS 2001: Current status and future directions, Meteorol. Atmos. Phys., 82, 5–29, 2003.
Deardorff, J. W.: The development of boundary layer turbulence models for use in studying the severe storm environment, Proceedings of the SESAME Opening Meeting, Boulder, NOAA-ERL, 251–264, 1975.
DeCaria, A. J., Pickering, K. E., Stenchikov, G. L., Scala, J. R., Stith, J. L., Dye, J. E., Ridley, B. A., and Laroche, P.: A cloud-scale model study of lightning-generated NO_x in an individual thunderstorm during STERAO-A, J. Geophys. Res., 105, 11 601–11 616, 2000.
DeCaria, A. J., Pickering, K. E., Stenchikov, G. L., and Ott, L. E.: Lightning-generated NO_x and its impact on tropospheric ozone production: A 3-D modeling study of a STERAO-A thunderstorm, J. Geophys. Res., 110, D14303, doi:10.1029/2004JD005556, 2005.
Dye, J. E., Ridley, B. A., Baumann, K., Skamarock, W. C., Barth, M. C., Venticinque, M., Defer, E., Blanchet, P., Thery, C., Laroche, P., Hubler, G., Parrish, D. D., Ryerson, T., Trainer, M., Frost, G., Holloway, J. S., Fehsenfeld, F. C., Tuck, A., Matejka, T., Bartels, D., Rutledge, S. A., Lang, T., Stith, J., and Zerr, R.: An Overview of the STERAO–Deep Convection Experiment with Results for the 10 July Storm, J. Geophys. Res., 105, 10 023–10 045, 2000.
Ekman, A., Wang, C., Ström, J., and Wilson, J.: Explicit simulation of aerosol physics in a

cloud-resolving model: A sensitivity study based on an observed convective cloud, Atmos. Chem. Phys., 4, 773–791, 2004, http://www.atmos-chem-phys.net/4/773/2004/.

Ekman, A., Wang, C., Ström, J., and Krejci, R.: Explicit simulation of aerosol physics in a cloud-resolving model: Aerosol transport and processing in the free troposphere; J. Atmos. Sci., 63, 682–696, 2006.

Fridlind, A. M., Ackerman, A. S., Jensen, E. J., Heymsfield, A. J., Poellot, M. R., Stevens, D. E., Wang, D., Miloshevich, L. M., Baumgardner, D., R. Lawson, P., Wilson, J. C., Flagan, R. C., Seinfeld, J. H., Jonsson, H. H., VanReken, T. M., Varutbangkul, V., and Rissman, T. A.: Evidence for the predominance of mid-tropospheric aerosols as subtropical anvil cloud nuclei. Science, 304, 718–722, doi:10.1126/science.1094947, 2004.

Fu, Q. and Liou, K. N.: Parameterization of the radiative properties of cirrus clouds, J. Atmos. Sci., 50, 2008–2025, 1993.

Grabowski, W. W.: Sixth WMO International Cloud Modeling Workshop, Bull. Am. Meteorol. Soc., 87, 639–642, 2006.

Helsdon Jr., J. H. and Farley, R. D.: A numerical modeling study of a Montana thunderstorm, 2, model results vs. observations involving electrical aspects. J. Geophys. Res., 92, 5661–5675, 1987.

Helsdon Jr., J. H., Wu, G., and Farley, R. D.: An intracloud lightning parameterization scheme for a storm electrification model. J. Geophys. Res., 97, 5865–5884, 1992.

Helsdon Jr., J. H., Wojcik, W. A., and Farley, R. D.: An examination of thunderstorm charging mechanisms using a two-dimensional storm electrification model. J. Geophys. Res., 106, 1165–1192, 2001.

Helsdon, Jr. J. H., Gattaleeradapan, S., Farley, R. D., and Waits, C. C.: An examination of the convective charging hypothesis: charge structure, electric fields, and Maxwell currents. J. Geophys. Res., 107(D22), 4630, doi:10.1029/2001JD001495, 2002.

Hindmarsh, A. C.: ODEPACK, A systematized collection of ODE solvers, in Scientific Computing, edited by R. S. Stepleman et al., 55–64, North-Holland, New York, 1983.

Houze Jr., R. A.: Cloud Dynamics, Academic Press, San Diego, 573 pp, 1993.

Jacobson, M. Z.: Computation of global photochemistry with SMVGEAR-II, Atmos. Environ., 29, 2541–2546, 1995.

Jaeglé, L., Jacob, D. J., Wang, Y., Weinheimer, A. J., Ridley, B. A., Campos, T. L., Sachse, G. W., and Hagen, D. E.: Sources and chemistry of NO_x in the upper troposphere over the

United States, Geophys. Res. Lett., 25, 1705–1708, 1998.
Jensen E. J., Ackerman, A. S., Stevens, D. E., Toon, O. B., and Minnis, P.: Spreading and growth of contrails in a sheared environment, J. Geophys. Res., 103, 31 557–31 567, 1998.
Kessler, E.: On the distribution and continuity of water substance in atmospheric circulations, Meteorol. Monogr., 10, No 32, 84 pp., 1969.
Klemp, J. B. and Wilhelmson, R. B.: Simulation of 3-dimensional convective storm dynamics, J. Atmos. Sci., 35, 1070–1096, 1978a.
Klemp, J. B. and Wilhelmson, R. B.: Simulations of right- and left-moving storms produced through storm splitting, J. Atmos. Sci., 35, 1097–1110, 1978b.
Lawrence, M. and Rasch, P. J.: Tracer transport in deep convective updrafts: Plume ensemble versus bulk formulations, J. Atmos. Sci., 62, 2880–2894, 2005.
Leriche, M., Cautenet, S., Barth, M., and Chaumerliac, N.: Modelling of the July 10 STERAO storm with the RAMS model: Chemical species redistribution including gas phase and aqueous phase chemistry, in Air Pollution Modeling and Its Application XVIII, edited by: Borrego, C. and Renner, E., pp. 433–442, Elsevier, Amsterdam, The Netherlands, 2007.
Lipps, F. B. and Hemler, R. S.: Numerical simulations of deep tropical convection associated with large-scale convergence, J. Atmos. Sci., 43, 1796–1816, 1986.
Lin, Y-L, Farley, R. D., and Orville, H. D.: Bulk parameterization of the snow field in a cloud model, J. Climate and Appl. Meteorol., 22, 1065–1092, 1983.
MacGorman, D. R. and Rust, W. D.: The Electrical Nature of Storms, Oxford University Press, 422 pp., 1998.
Madronich S.: Photodissociation in the atmosphere: 1. Actinic fluxes and the effects of ground reflections and clouds. J. Geophys. Res., 92, 9740–9752, 1987.
Meyers, M. P., Walko, R. L., Harrington, J. Y., and Cotton, W. R.: New RAMS cloud microphysics parameterization. Part II: The two moment scheme, Atmos. Res., 45, 3–39, 1997.
Pickering K. E., Thompson, A. M., Wang, Y. S., Tao, W. K., McNamara, D. P., Kirchhoff, V. W. J. H., Heikes, B. G., Sachse, G. W., Bradshaw, J. D., Gregory, G. L., and Blake, D. R.: Convective transport of biomass burning emissions over Brazil during TRACE A, J. Geophys. Res., 101, 23 993–24 012, 1996.
Pickering, K. E., Wang, Y., Tao, W-K, Price, C., and Müller, J.-F.: Vertical distributions of lightning NO_x for use in regional and global chemical transport models, J. Geophys. Res., 103, 31 203–31 212, 1998.
Pinty, J.-P. and Jabouille, P.: A mixed-phase cloud parameterization for use in a mesoscale

non-hydrostatic model: Simulations of a squall line and of orographic precipitation, In Conf. On Cloud Physics, Everett, WA, Am. Meteorol. Soc., 217–220, 1998.
Popp, P. J. Gao, R. S., Marcy, T. P., Fahey, D. W., Hudson, P. K., Thompson, T. L., Kärcher, B., Ridley, B. A., Weinheimer, A. J., Knapp, D. J., Montzka, D. D., Baumgardner, D., Garrett, T. J., Weinstock, E. M., Smith, J. B., Sayres, D. S., Pittman, J. V., Dhaniyala, S., Bui, T. P., and Mahoney, M. J.: Nitric acid uptake on subtropical cirrus cloud particles, J. Geophys. Res., 109, doi:10.1029/2003JD004255, 2004.
Price, C., Penner, J., and Prather, M.: NO_x from lightning 1. Global distribution based on lightning physics, J. Geophys. Res., 102, 5929–5941, 1997.
Ridley, B. A., Walega, J. G., Dye, J. E., and Grahek, F. E.: Distributions of NO, NO_x, NO_y, and O_3 to 12 km altitude during the summer monsoon season over New Mexico, J. Geophys. Res., 99, 25 519–25 534, 1994.
Rutledge, S. A., Hegg, D. A., and Hobbs, P. V.: A numerical model for sulfur and nitrogen scavenging in narrow cold-frontal rainbands, 1, Model description and discussion of microphysical fields, J. Geophys. Res., 91, 14 385–14 402, 1986.
Schwartz, S. E.: Mass-transport considerations pertinent to aqueous phase reactions of gases in liquid-water clouds, in Chemistry of Multiphase Atmospheric Systems, Ed. W. Jaeschke, Springer-Verlag, New York, 415–471, 1986.
Seinfeld, J. H. Atmospheric Chemistry and Physics of Air Pollution, John Wiley & Sons, New York, 768 pp, 1986.
Seifert A. and Weisman, M.: A comparison of bulk microphysical schemes for cloud resolving NWP, in Proceedings of the 6th WRF / 15th MM5 Users' Workshop, Boulder, Colorado, http://www.mmm.ucar.edu/wrf/users/workshops/WS2005/abstracts/Session6/2-Seifert.pdf, 2005.
Skamarock, W. C., Powers, J., Barth, M. C., Dye, J. E., Matejka, T., Bartels, D., Baumann, K., Stith, J., Parrish, D. D., and Hubler, G.: Numerical simulations of the 10 July STERAO/Deep Convection Experiment Convective System: Kinematics and transport, J. Geophys. Res., 105, 19 973–19 990, 2000.
Skamarock, W. C., Dye, J. E., Defer, E., Barth, M. C., Stith, J. L., Ridley, B. A., and Baumann, K.: Observational- and Modeling-Based budget of lightning-produced NO_x in a continental thunderstorm, J. Geophys. Res., 108(D10), 4305, doi10.1029/2002JD002163, 2003.
Skamarock, W. C, Klemp, J. B., Dudhia, J., Gill, D., Barker, D., Wang, W., and Powers, J. G.: A description of the Advanced Research WRF Version 2.., Technical Note NCAR/TN-468+STR, NCAR, Boulder, Colorado, 2005.

Smolarkiewicz, P. K.: A full multidimensional positive definite advection transport algorithm with small implicit diffusion, J. Comput. Phys., 65, 325–363, 1984.
Smolarkiewicz, P. K. and Clark, T. L.: The multidimensional positive definite advection transport algorithm. Further development and applications, J. Comput. Phys., 67, 394–439, 1986.
Smolarkiewicz, P. K. and Grabowski, W. W.: The multidimensional positive advection transport algorithm: Nonoscillatory option, J. Comp. Phys., 86, 355–375, 1990.
Soong, S.-T. and Ogura, Y.: Response of trade wind cumuli to large-scale processes, J. Atmos. Sci., 37, 2035–2050, 1980.
Spiridonov, V. and Curic, M.: A three-dimensional numerical simulation of sulfate transport and redistribution, Can. J. Phys., 81, 1067–1094, 2003.
Spiridonov, V. and Curic, M.: The relative importance of scavenging, oxidation, and ice-phase processes in the production and wet deposition of sulfate, J. Atmos. Sci., 62, 2118–2135, 2005.
Stenchikov, G., Dickerson, R., Pickering, K., Ellis, W., Doddridge, B., Kondragunta, S., Poulida, O., Scala, J., and Tao, W. K.: Stratosphere-troposphere exchange in a midlatitude mesoscale convective complex .2. Numerical simulations, J. Geophys. Res., 101, 6837–6851, 1996.
Stevens D. E. and Bretherton C. S.: A forward-in-time advection scheme and adaptive multilevel flow solver for nearly incompressible atmospheric flow, J. Comp. Phys., 129, 284–295, 1996.
Stickler, A., Fischer, H., Williams, J., de Reus, M., Sander, R., Lawrence, M. G., Crowley, J. N., and Lelieveld, J.: Influence of summertime deep convection on formaldehyde in the middle and upper troposphere over Europe, J. Geophys. Res., 111, D14308, doi:10.1029/2005JD007001, 2006.
Taghavi, M., Cautenet, S., and Foret, G.: Simulation of ozone production in a complex circulation region using nested grids, Atmos. Chem. Phys., 4, 825–838, 2004, http://www.atmos-chem-phys.net/4/825/2004/.
Tao, W-.K. and Simpson, J.: Goddard Cumulus Ensemble model. Part I: Model description, TAO, 4, 35–72, 1993.
Tao, W.-K., Simpson, J., Baker, D., Braun, S., Chou, M.-D., Ferrier, B., Johnson, D., Khain, A., Lang, S., Lynn, B., Shie, C.-L., Starr, D., Sui, C.-H., Wang, Y., and Wetzel, P.: Microphysics, radiation, and surface processes in the Goddard Cumulus Ensemble (GCE) model, Meteorol. Atmos. Phys., 82, 97–137, 2001.
Taylor, G. R.: Sulfate Production and Deposition in Midlatitude Continental Cumulus Clouds. Part II: Chemistry Model Formulation and Sensitivity Analysis, J. Atmos. Sci., 46, 1991–2007,

1989.
Tost, H., Jockel, P., and Lelieveld, J.: Influence of different convection parameterizations in a GCM, Atmos. Chem. Physics, 6, 5475–5493, 2006.
Tripoli, G. J. and Cotton, W. R.: The use of ice-liquid water potential temperature as a thermodynamical variable in deep atmospheric models, Mon. Weather Rev., 109, 1094–1102, 1981.
Wang, C.: A modeling study on the response of tropical deep convection to the increase of CCN concentration. 1. Dynamics and microphysics, J. Geophys. Res., 110, D21211, doi:10.1029/2004JD005720, 2005a.
Wang, C.: A modeling study on the response of tropical deep convection to the increase of CCN concentration. 2. Radiation and chemistry, J. Geophys. Res., 110, D22204, doi:10.1029/2005JD005829, 2005b.
Wang, C. and Chang, J.: Three-dimensional numerical model of cloud dynamics, microphysics, and chemistry 1. Concepts and formulation, J. Geophys. Res., 98(D8), 14 827–14 844, 1993a.
Wang, C. and Chang, J.: A three-dimensional numerical model of cloud dynamics, microphysics, and chemistry 3. Redistribution of pollutants, J. Geophys. Res., 98(D9), 16 787–16 798, 1993b.
Wang, C. and Chang, J.: A three-dimensional numerical model of cloud dynamics, microphysics, and chemistry 4. Cloud chemistry and precipitation chemistry, J. Geophys. Res., 98(D9), 16 799–16 808, 1993c.
Wang, C. and Crutzen, P. J.: Impact of a simulated severe local storm on the redistribution of sulfur dioxide. J. Geophys. Res., 100(D6), 11 357–11 367, 1995.
Wang, C. and Prinn, R.: On the roles of deep convective clouds in tropospheric chemistry, J. Geophys. Res., 105(D17), 22 269–22 298, 2000.
Wang, C., Prinn, R. G., Sokolov, A.: A global interactive chemistry and climate model: Formulation and testing, J. Geophys. Res., 103(D3), 3399–3418, 1998a.
Wang, Y., DeDilva, A. W., Goldenbaum, G. C., and Dickerson, R. R.: Nitric oxide production by simulated lightning: dependence on current, energy, and pressure, J. Geophys. Res., 103(D15), 19 149–19 160, doi:10.1029/98JD01356, 1998b.
Wicker, L. J. and Skamarock, W. C.: Time-splitting methods for elastic models using forward time schemes, Mon. Weather Rev., 130, 2088–2097, 2002.
Xie, S; Xu, K-M, Cederwall, R. T., Bechtold, P., Genio, A. D. D., Klein, S. A., Cripe, D. G., Ghan,

S. J., Gregory, D., Iacobellis, S. F., Krueger, S. K., Lohmann, U., Petch, J. C., Randall, D. A., et al.: Intercomparison and evaluation of cumulus parametrizations under summertime midlatitude continental conditions, Q. J. R. Meteorol. Soc., 128, 1095–1135, 2002.

Zhang, X., Helsdon Jr., J. H., and Farley, R. D.: Numerical modeling of lightning-produced NO_x using an explicit lightning scheme: 2. three-dimensional simulation and expanded chemistry. J. Geophys. Res., 108(D18), 4580, doi:10.1029/2002JD003225, 2003.

Table 1. Description of the model dynamics, microphysics and configuration used for the simulations.

Model	Dynamics, Thermodynamics, Radiation	Cloud Microphysics and Aerosols	Configuration
WRF-AqChem (Barth, Kim)	3-D, flux-form, Runge-Kutta no radiation	2 liquid, 3 ice, predict M (Lin et al, 1983) hail characteristics no aerosols	160×160×20 km^3 1×1 km^2 horizontal 50 vertical levels 10 s time step
C. Wang	3-D pseudo-elastic, ice-liquid T interactive radiation	2 liquid, 2 ice, predict N and M graupel characteristics, Prognostic CCN and IN	145×120×20 km^3 1×1×0.4 km^3 resol. 3 s time step
U. Md/GCE (Pickering, Ott, Stenchikov)	3d GCE Model (Tao and Simpson, 1993)	2 liquid, 3 ice, predict M (Lin et al., 1983) hail characteristics no aerosols	360×328×25 km^3 2×2×0.5 km^3 resol. 3, 15, and 30 s time step
RAMS (Leriche, Cautenet)	3-D, anelastic interactive radiation	2 liquid, 3 ice, predict N and M (Meyers et al., 1997) hail characteristics no aerosols	120×120×20 km^3 1×1 km^2 resolution 51 vertical levels 5 s time step
Meso-NH (Pinty, Barthe Mari)	3-D, anelastic MPDATA advection no radiation	2 liquid, 3 ice, predict M (Pinty and Jabouille, 1998) graupel characteristics no aerosols	160×160×25 km^3 1×1 km^2 resolution 50 vertical levels 2 s time step
SDSMT (Helsdon, Farley)	3-D, modified Clark-Hall MPDATA advection of scalars no radiation	2 liquid, 3 ice, predict M (Lin et al, 1983) hail characteristics no aerosols	120×120×20 km^3 1×1×0.25 km^3 resol. 2 s time step
DHARMA (Fridlind, Ackerman)	3D large eddy simulation no radiation	Sectional aerosols, cloud liquid, and cloud ice (16 bins each) graupel characteristics	120×120×20 km^3 1×1×0.25 km^3 resol. 0.2–5.0 s time step
V. Spiridonov (Spiridonov, Telenta)	3-D, Klemp-Wilhelmson dynamics no radiation	2 water, 3 ice, predict M (modified Lin et al., 1983) hail characteristics no aerosols	140×140×15 km^3 1×1×0.5 km^3 resol. 10 s time step

ACPD
7, 8035–8085, 2007

Table 2. Description of chemistry-related processes used by each model.

Model	Chemistry and $L(NO_x)$	Gas-Aqueous Transfer*	Chemistry-microphysics
WRF-AqChem (Barth, Kim)	Online chem.. $L(NO_x)$ (DeCaria et al., 2005)	Hybrid K_H and diffusion-limited mass transfer	Retain species during freezing
C. Wang	Online chem. $L(NO_x)$ (Wang and Prinn, 2000)	Diffusion-limited mass transfer	Retain
U. Md / GCE (Pickering, Ott, Stenchikov)	Offline gas chem. $L(NO_x)$ (DeCaria et al., 2005)	K_H	Species removed by liquid hydrometeors only
RAMS (Leriche, Cautenet)	Online chem. $L(NO_x)$ (Pickering et al., 1998)	Diffusion-limited mass transfer	Degas
Meso-NH (Pinty, Barthe, Mari)	Scav. of soluble species Explicit electrical scheme (Barthe et al., 2005, 2007)	Diffusion-limited mass transfer	Degas
SDSMT (Helsdon, Farley)	Online gas chem. Explicit electrical scheme (Helsdon et al., 2001; 2002)	None	None
DHARMA (Fridlind, Ackerman)	None	None	None
V. Spiridonov	Tracers and aqueous chem. No $L(NO_x)$	K_H	Retain

*K_H indicates that Henry's law equilibrium is used to partition between gaseous and aqueous phases.

ACPD
7, 8035–8085, 2007

Table 3. Anvil Cross-Sectional Area, Dry Air Mass Flux Density, and Species Flux Density from Each Model Simulation Averaged over a 1 Hour Time Period.

Model	Anvil Area (10^6 m^2)	Mass Flux (kg m^{-2} s^{-1})	CO Flux (10^{-5} mol m^{-2} s^{-1})	NO_x Flux (10^{-8} mol m^{-2} s)
Observations	315	5.9	1.90	5.8*
WRF-AqChem	187.7	6.75	1.94	7.23
C. Wang	442.7	6.72	1.94	5.97
U. Md/GCE	274.0	9.06	2.54	8.45
RAMS	332.7	7.68	2.29	5.30
Meso-NH	590.0	6.73	1.93	3.93
SDSMT	196.9	6.59	1.93	13.04
DHARMA	382.2	8.13	2.35	4.28
V. Spiridonov	109.0	9.13	2.79	2.66
*avg +/– std dev	314.4 +/– 156.3	7.60 +/– 1.07	2.21 +/– 0.33	6.36 +/– 3.27

Values from simulations are time averages from t = 3600 to t = 7200 s of the integration, sampled at 10 min intervals. DHARMA and Spiridonov models do not include lightning production of NO.
*The NO_x flux from the observations assumes NO_x = 1.3 NO.

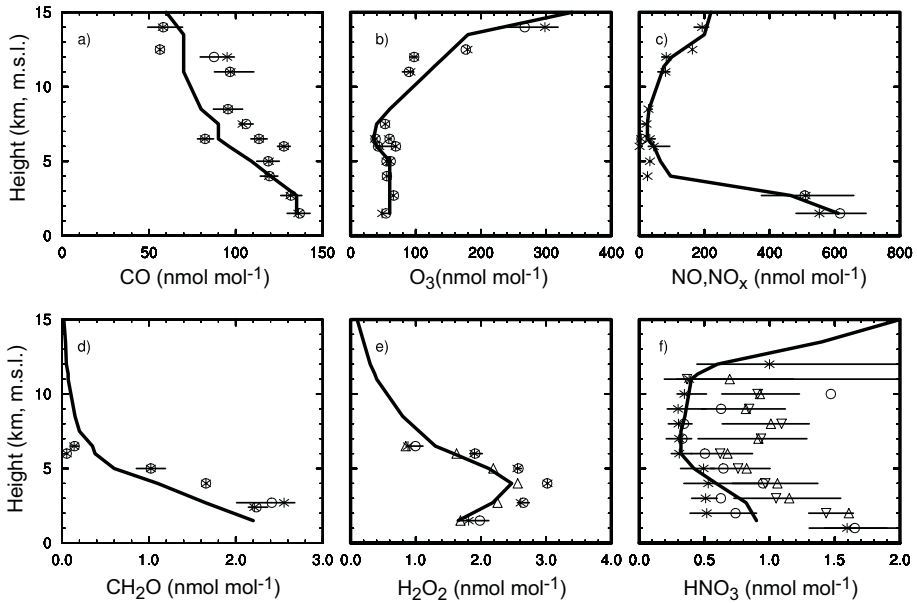

Fig. 1. Initial profiles (black lines) of the chemical species simulated in the case. Circles (average) and asterisks (median) points are from aircraft (UND Citation above 5 km m.s.l.; NOAA WP3D below 7 km m.s.l.) observations outside of cloud near the 10 July 1996 storm. In panel **(c)**, the points are NO mixing ratios and the lines are NO_x mixing ratios. On the H_2O_2 profile plot **(e)**, points are for total peroxide measurements except for the triangles which are for 0.85 times the total peroxide. Circles (average) and asterisks (median) on the HNO_3 profile plot **(f)** are from NOy measurements taken aboard the NASA DC8 during the SUCCESS field campaign in April–May 1996. Triangles (average) and nablas (median) on the HNO_3 profile plot (f) are from NOy measurements taken aboard the NCAR Sabreliner during the ELCHEM field campaign in August 1989.

ACPD
7, 8035–8085, 2007

EGU

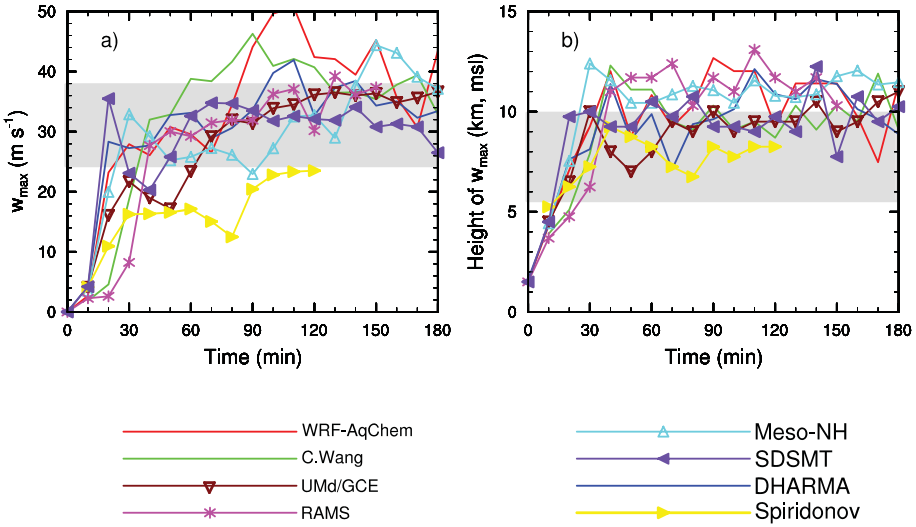

Fig. 2. **(a)** Peak updraft speed and **(b)** height of peak updraft from each of the simulations. Gray shaded regions represent observed values derived from the CHILL radar (W. Deierling, personal communication).

ACPD
7, 8035–8085, 2007

EGU

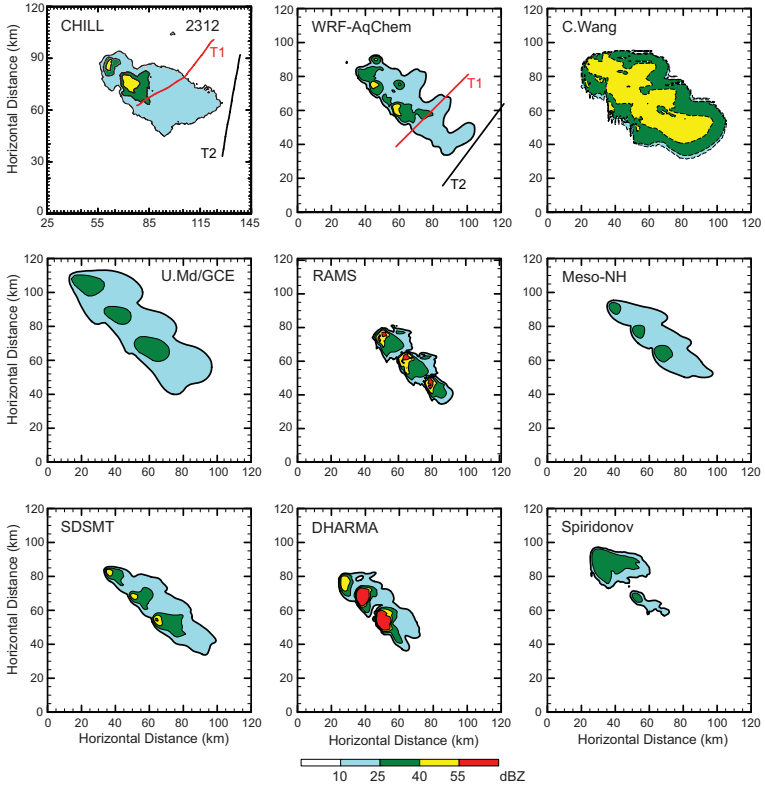

Fig. 3. Radar reflectivity (dBZ) at z = 10.5 km m.s.l. Observations (upper left panel) from CSU CHILL radar at 2312 UTC. Model results at t = 1 h from WRF-AqChem, C. Wang, UMd/GCE, RAMS, Meso-NH, SDSMT, DHARMA, and Spiridonov models. T1 and T2 lines in the CHILL panel represent the actual flight track for the two transects shown in subsequent figures. T1 and T2 lines in the WRF-AqChem panel represent the location of the modeled transects shown in the same subsequent figures.

ACPD
7, 8035–8085, 2007

EGU

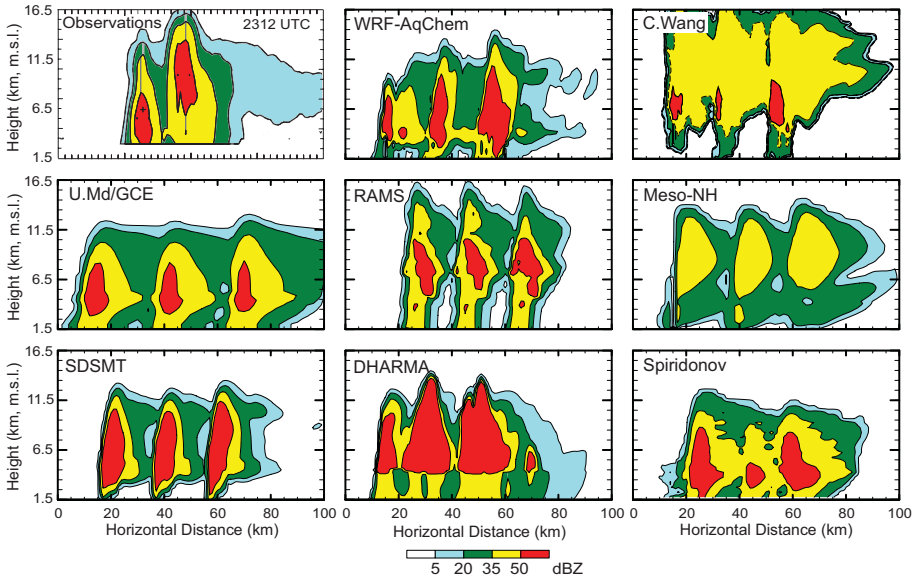

Fig. 4. Radar reflectivity (dBZ) along the NW-SE vertical cross-section. Observations (upper left panel) from CSU CHILL radar at 23:12 UTC. Model results at t = 1 h from WRF-AqChem, C. Wang, UMd./GCE, RAMS, Meso-NH, SDSMT, DHARMA and Spiridonov models.

ACPD
7, 8035–8085, 2007

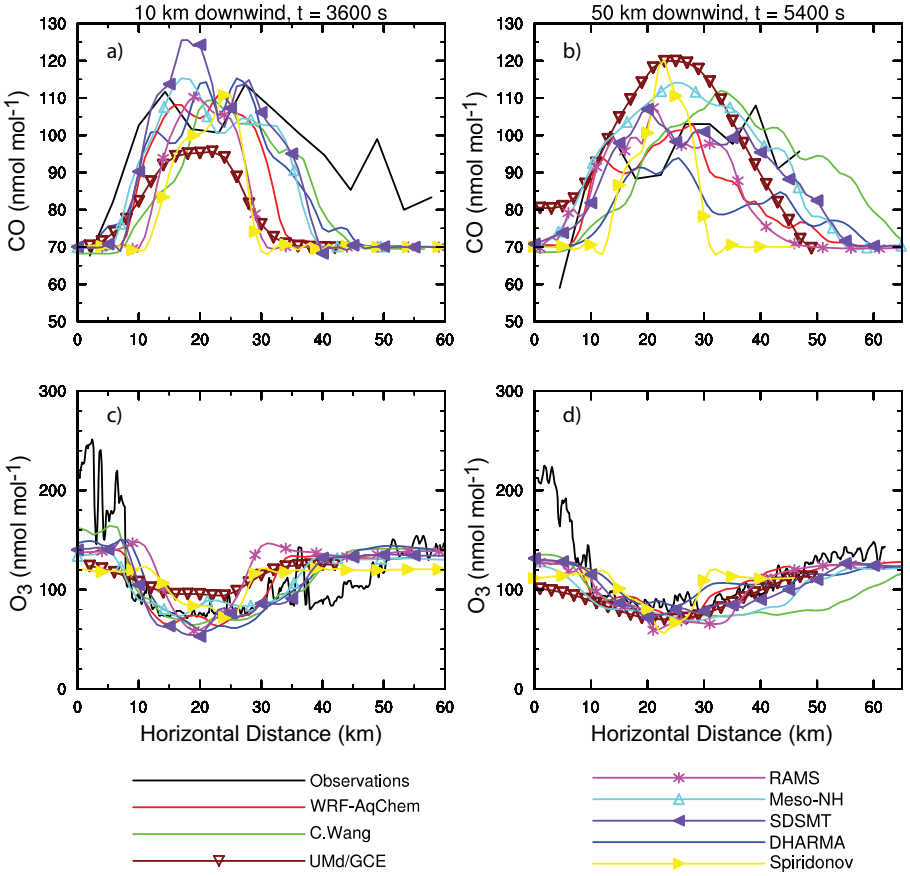

Fig. 5. CO and O_3 measurements (black lines) from the UND-Citation aircraft for across-anvil transects at 10 km downwind of the south-easternmost convective cell and 11.6 km m.s.l. (left panels) and at 50 km downwind of the south-easternmost convective cell and 11.2 km m.s.l. (right panels). Results from model calculations are plotted along these transects.

ACPD
7, 8035–8085, 2007

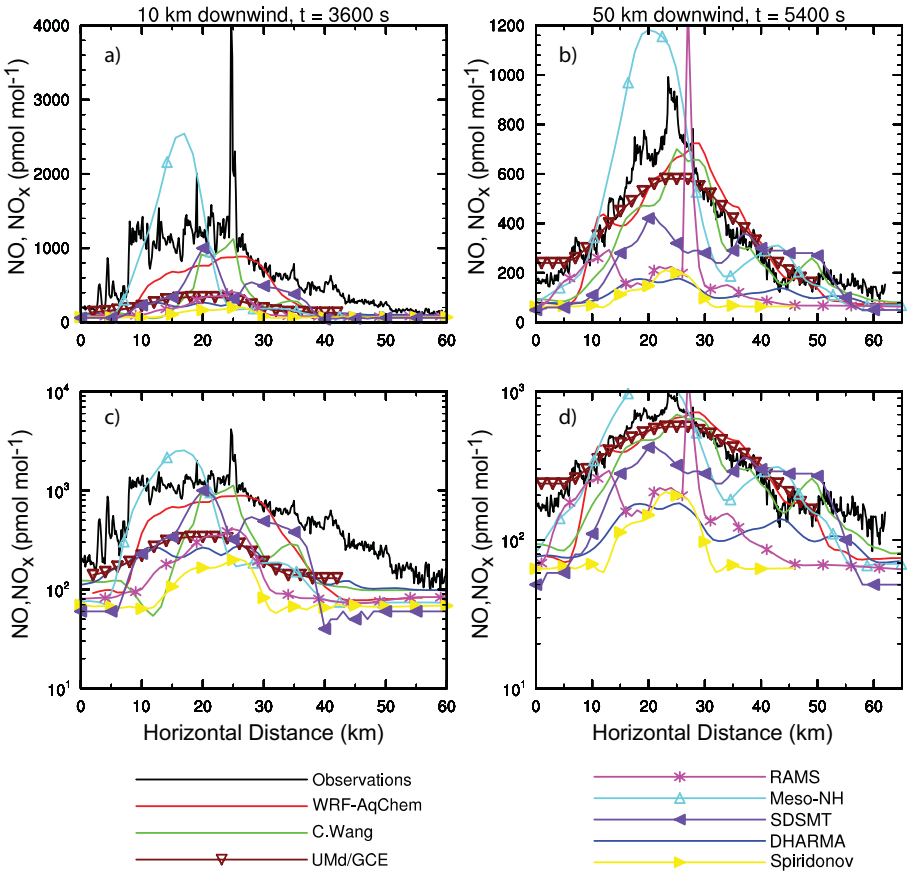

Fig. 6. NO measurements (black lines) from the UND-Citation aircraft for across-anvil transects at 10 km downwind of the south-easternmost convective cell and 11.6 km m.s.l. (left panels) and at 50 km downwind of the south-easternmost convective cell and 11.2 km m.s.l. (right panels). Results from model calculations of NO_x are plotted along these transects. NO_x is plotted on a linear scale in the upper panels, and on a logarithmic scale in the lower panels.

ACPD
7, 8035–8085, 2007

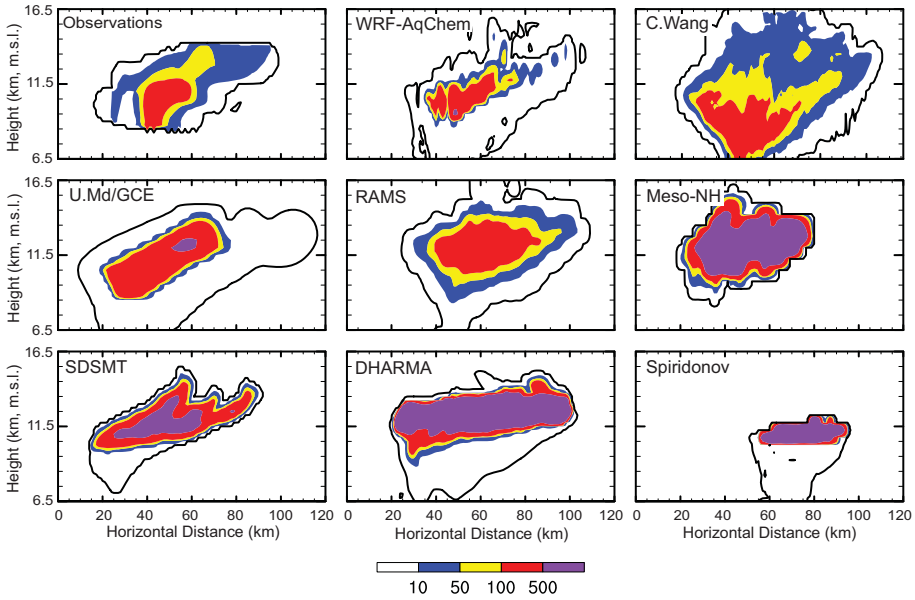

Fig. 7. Cloud particle concentration (per liter) across the anvil at t = 2316 to t = 00:36 UTC for the observations and t = 6000 s for the model results. The solid black line is cloud particle concentration equal to 0.1 per liter. Objective analysis of the aircraft measurements (upper left panel) are from Skamarock et al. (2003). Model results are for the WRF-AqChem, C. Wang, UMd/GCE, RAMS, Meso-NH, SDSMT, DHARMA, and Spiridonov models.

ACPD
7, 8035–8085, 2007

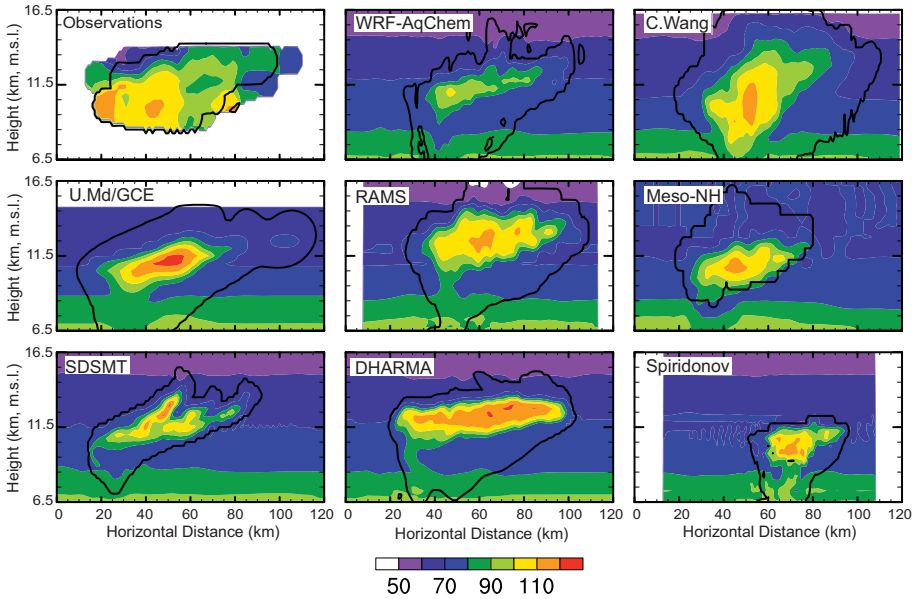

Fig. 8. Same as Fig. 7 except for CO (nmol mol^{-1}). The solid black line is cloud particle concentration equal to 0.1 per liter.

ACPD
7, 8035–8085, 2007

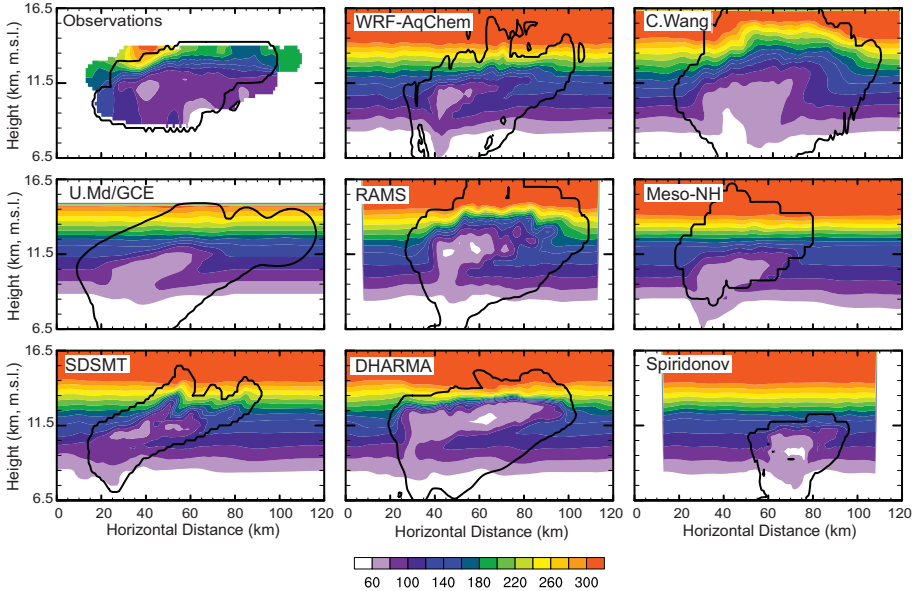

Fig. 9. Same as Fig. 7 except for O_3 (nmol mol^{-1}). The solid black line is cloud particle concentration equal to 0.1 per liter.

ACPD
7, 8035–8085, 2007

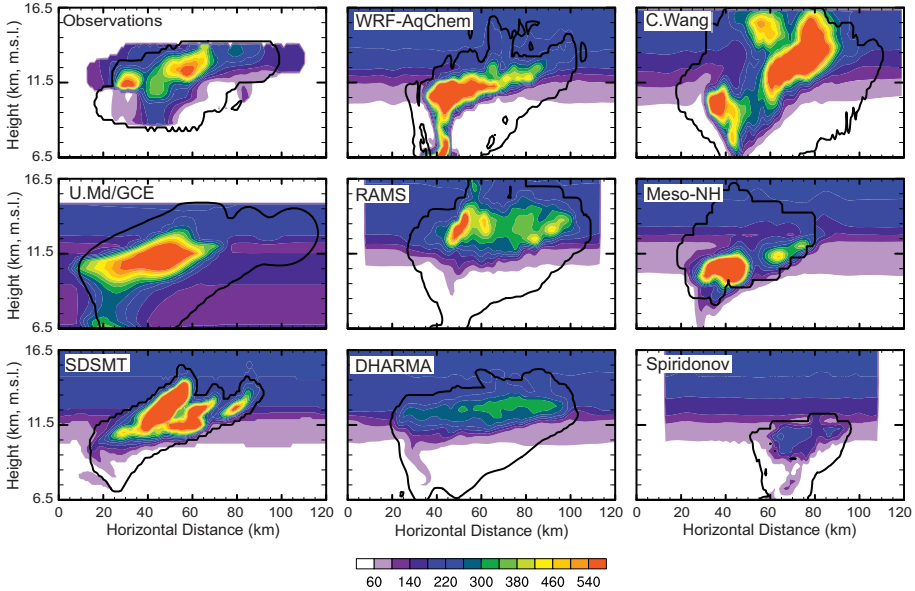

Fig. 10. Same as Fig. 7 except for NO, NO_x. Observations show NO mixing ratios (pmol mol^{-1}) and models show NO_x. The solid black line is cloud particle concentration equal to 0.1 per liter.

ACPD
7, 8035–8085, 2007

EGU

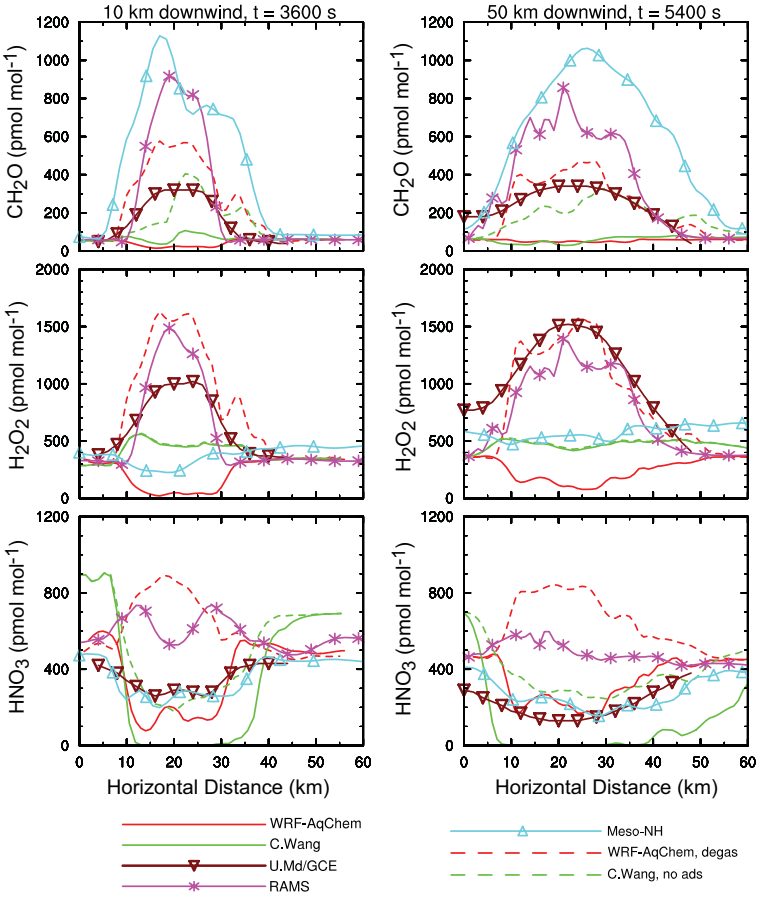

Fig. 11. CH_2O, H_2O_2, and HNO_3 mixing ratios from different models for across-anvil transects at 10 km downwind of the south-easternmost convective cell and 11.6 km m.s.l. (left panels) and at 50 km downwind of the south-easternmost convective cell and 11.2 km m.s.l. (right panels).

ACPD
7, 8035–8085, 2007